PL-TR--
95-1079

MATERIALS FOR THERMIONIC POWER SYSTEMS

Ralph Zee, Ph.D.
Bryan A. Chin
Fefrey Fergus
M. Frank Rose

Auburn University
College of Engineering and
Engineering Experiment Station
Materials Research and Education Center
201 Ross Hall
Auburn University, Alabama 36849-5341

October 1995

Final Report

PHILLIPS LABORATORY
Space and Missiles Technology Directorate
AIR FORCE MATERIEL COMMAND
KIRTLAND AIR FORCE BASE, NM 87117-5776

PL-TR-95-1079

This final report was prepared by Auburn University for ORION International Technologies, Albuquerque, New Mexico, under Contract F29601-89-C-0001. The Laboratory Project Officer in charge was Dr. Michael Schuller, VTP.

When Government drawings, specifications, or other data are used for any purpose other than in connection with a definitely government-related procurement, the United States Government incurs no responsibility or any obligation whatsoever. The fact that the Government may have formulated or in any way supplied the said drawings, specification or other date, is not go be regarded by implication, or otherwise in any manner construed, as licensing the holder, or an other person or corporation; or as conveying any rights or permission to manufacture, use, or sell any patented invention that may in any way be related thereto.

This report has been authored by a contractor of the United States Government. Accordingly, the United States Government retains a nonexclusive, royalty-free license to publish or reproduce the material contained herein, or allow others to do so, for the United States Government purposes.

If you address has changed, if you wish to be removed from the mailing list, or if your organization no longer employs the addressee, please notify PL/NTS, Kirtland AFB, NM 87117-6008 to help maintain a current mailing list.

This report has been reviewed and is approved for publication.

MICHAEL SCHULLER, GS-13, DAF
Chief, Space Power Laboratory

FOR THE COMMANDER

DAVID H. KRISTENSEN, Lt. Col, USAF
Chief, Power and Thermal Management Division

HENRY L. PUGH, JR, Col, USAF
Director, Space and Missile Technology Directorate

DO NOT RETURN COPIES OF THIS REPORT UNLESS CONTRACTUAL OBLIGATIONS OR NOTICE ON A SPECIFIC DOCUMENT REQUIRES THAT IT BE RETURNED.

The following notice applies to any unclassified (including originally classified and now declassified) technical reports released to "qualified U.S. contractors" under the provisions of DoD Directive 5230.25, Withholding of Unclassified Technical Data From Public Disclosure.

NOTICE TO ACCOMPANY THE DISSEMINATION OF EXPORT-CONTROLLED TECHNICAL DATA

1. Export of information contained herein, which includes, in some circumstances, release to foreign nationals within the United States, without first obtaining approval or license from the Department of State for items controlled by the International Traffic in Arms Regulations (ITAR), or the Department of Commerce for items controlled by the Export Administration Regulations (EAR), may constitute a violation of law.

2. Under 22 U.S.C. 2778 the penalty for unlawful export of items or information controlled under the ITAR is up to two years imprisonment, or a fine of $100,000, or both. Under 50 U.S.C., Appendix 2410, the penalty for unlawful export of items or information controlled under the EAR is a fine of up to $1,000,000, or five times the value of the exports, whichever is greater; or for an individual, imprisonment of up to 10 years, or a fine of up to $250,000, or both.

3. In accordance with your certification that establishes you as a "qualified U.S. Contractor", unauthorized dissemination of this information is prohibited and may result in disqualification as a qualified U.S. contractor, and may be considered in determining your eligibility for future contracts with the Department of Defense.

4. The U.S. Government assumes no liability for direct patent infringement, or contributory patent infringement or misuse of technical data.

5. The U.S. Government does not warrant the adequacy, accuracy, currency, or completeness of the technical data.

6. The U.S. Government assumes no liability for loss, damage, or injury resulting from manufacture or use for any purpose of any product, article, system, or material involving reliance upon any or all technical data furnished in response to the request for technical data.

7. If the technical data furnished by the Government will be used for commercial manufacturing or other profit potential, a license for such use may be necessary. Any payments made in support of the request for data do not include or involve any license rights.

8. A copy of this notice shall be provided with any partial or complete reproduction of these data that are provided to qualified U.S. contractors.

D E S T R U C T I O N N O T I C E

For classified documents, follow the procedures in DoD 5200.22-M, Industrial Security Manual, Section II-19 or DoD 5200.1-R, Information Security Program Regulation, Chapter IX. For unclassified, limited documents, destroy by any method that will prevent disclosure of contents or reconstruction of the document.

DRAFT SF 298

1. Report Date (dd-mm-yy) October 1995	2. Report Type Final	3. Dates covered (from... to) 01/9 to 10/95
4. Title & subtitle Materials for Thermionic Power Systems		5a. Contract or Grant # F29601-89-C-0001
		5b. Program Element # 62601F
6. Author(s) Ralph Zee, Ph.D. Bryan A. Chin Fefrey Fergus M. Frank Rose		5c. Project # 2218
		5d. Task # TE
		5e. Work Unit # AC

7. Performing Organization Name & Address Auburn University College of Engineering and Engineering Experiment Station Materials Research and Education Center 201 Ross Hall, Auburn University, AL 36849-5341	8. Performing Organization Report #
9. Sponsoring/Monitoring Agency Name & Address Phillips Laboratory 3550 Aberdeen Ave SE Kirtland AFB, NM 87117-5776	10. Monitor Acronym
	11. Monitor Report # PL-TR-95-1079

12. Distribution/Availability Statement
Distribution authorized to U.S. Government Agencies and their contractors only; Critical Technology; October 1995. Other requests for this document shall be referred to AFMC/STI.

13. Supplementary Notes

14. Abstract Research efforts in this three month project have been devoted to the study of materials for space power applications. In particular, three aspects of materials were investigated: (Task #1) radiation induced conductivity in ceramic insulators at elevated temperature, (Task #2) growth of refractory alloy single crystals, and (Task #3) processing of ductile beta alumina. In the area of ceramic insulators, studies have shown that the electrical resistivity of insulators such as alumina can be significantly degraded when irradiated while subject to a bias voltage at elevated temperatures. This degradation process must be understood in order to alleviate the problem of insulator breakdown. The successful development of these refractory alloy single crystals will make an impact on advanced technologies other than the nuclear and aerospace areas. These crystals possess superior high temperature mechanical and environmental stabilities (relatively inert due to the absence of grain boundaries) which are required in numerous commercial

15. Subject Terms Interface radiation induced activity, ceramic insulators , alloy single crystals, ductile beta alumina

Security Classification of			19. Limitation of Abstract	20. # of Pages	21. Responsible Person (Name and Telephone #)
16. Report unclassified	17. Abstract unclassified	18. This Page unclassified	Limited	72	Mike Schuller (505) 846-0521

CONTENTS

FIGURES

FIGURES (Continued)

FIGURES (Concluded)

TABLES

1.0 OVERVIEW

Three aspects of materials relevant to space power systems were investigated in this three month project. The three issues addressed the mechanisms governing electrical degradation of ceramic insulators due to irradiation, the processing characteristics of refractory alloy single crystals and the feasibility of fabricating ductile beta alumina. The primary effort was concentrated in the first two areas.

Studies have shown that the electrical resistivity of insulators such as alumina can be significantly degraded when irradiated while subject to a bias voltage at elevated temperatures. This investigation examined the effects of radiation induced conductivity and electrical degradation in polycrystalline alumina and sapphire. Experiments were carried out at temperatures up to 823 K and an applied electric field of 500 kV/m. Effects of proton, alpha and gamma radiations were examined. Experimental results show that radiation induced conductivity (RIC) in alumina consists of recoverable and permanent contributions when irradiated with charged particles. These two radiation induced effects are not completely separable and are both functions of irradiation dose. In polycrystalline alumina, a significant increase in the permanent conductivity was observed after an incubation dose of 10^{-4} dpa (displacements per atom). However, only limited permanent electrical degradation was observed in single crystal samples at three times this damage level indicating the importance of grain boundaries in the radiation induced electrical degradation (RIED) process. Results from Rutherford Backscattered Spectroscopy (RBS) confirm that radiation enhanced diffusion of the gold contact is responsible for the degradation observed in the polycrystalline alumina specimens.

The effects of scan rate on both the solute segregation and the crystal growth characteristics in Mo-Nb, Mo-Hf and Mo-Hf-C alloys were also examined in this

study. Little difficulty was encountered when growing Mo-Nb alloys. The ease of crystal growth in Mo-Nb binary system was attributed to the small temperature difference between the solidus and the liquidus lines and the complete solid solution characteristics of the Mo-Nb system (the Mo-Nb system does not contain any intermetallic compound). A scan rate of 55 mm/hour was found to be suitable for producing satisfactory single crystals of Mo-11%Nb. However, for the Mo-Hf alloys, the highest scan rates for single crystal formation were found to depend on Hf content in an inverse manner. Experimental results show that the critical maximum scan rates for Mo-3.75%Hf alloy and Mo-5%Hf alloy are 11 mm/hour and 2 mm/hour, respectively. On the contrary, the rate of scan must be kept above 22 mm/hour to avoid serious solute segregation in Mo-Hf alloy single crystals. Based on these criteria, the optimum hafnium content was found to be 2.8%.

Finally, a feasibility study was conducted to identify means to fabricate more ductile beta alumina for high temperature applications. Samples of alumina with small amounts of zirconia were fabricated based on a powder metallurgy method.

2.0 INTRODUCTION

Research efforts in this three month project have been devoted to the study of materials for space power applications. In particular, three aspects of materials were investigated: (Task #1) radiation induced conductivity in ceramic insulators at elevated temperature, (Task #2) growth of refractory alloy single crystals, and (Task #3) processing of ductile beta alumina. In the area of ceramic insulators, studies have shown that the electrical resistivity of insulators such as alumina can be significantly degraded when irradiated while subject to a bias voltage at elevated temperatures. This degradation process must be understood in order to alleviate the problem of insulator breakdown. The successful development of these refractory alloy single crystals will make an impact on advanced technologies other than the nuclear and aerospace areas. These crystals possess superior high temperature mechanical and environmental stabilities (relatively inert due to the absence of grain boundaries) which are required in numerous commercial applications. Finally, the feasibility of fabricating ductile beta alumina for direct conversion applications was also examined. This final report is divided into three sections in accordance with these three tasks. Section 3 presents the results for task #1, Section 4 for task #2, and Section 5 for task #3.

3.0 RADIATION INDUCED ELECTRICAL CONDUCTIVITY IN INSULATORS

Many physical properties of alumina such as electrical conductivity, thermal conductivity, dielectric constants and loss tangent can be degraded at radiation damage levels well below one dpa, whereas severe mechanical damage happens only after several dpa or tens of dpa in alumina [1,2]. Of all the physical properties, the electrical resistivity or conductivity is of particular importance to insulators and is therefore the subject of this report. Radiation induced conductivity (RIC) is a well documented phenomenon [1-12]. This phenomenon has been observed extensively in ceramic materials including alumina [3], when these insulating materials are exposed to x-ray, gamma, electron, proton and neutron radiation. RIC has been found to be a very complex function of radiation flux, radiation temperatures and the materials involved according to numerous experimental results such as those obtained by Pells and Klaffky [2,4].

3.1 BACKGROUND

Investigations of the dependence of RIC on irradiation temperature by Klaffky [4] showed that there were regions in which RIC increased rapidly with temperature and regions in which it slowly decreased with temperature. A trap or thermal quenching theory has been established to explain this phenomenon. The essence of the model is that the free electrons and/or holes may be released from the trapping sites by thermal excitation [2]. Conditions for steady state radiation induced conductivity have been predicted from the model and the results show a very good agreement (within a factor of two) with the experimental findings.

The radiation induced electrical degradation or RIED has been a very controversial topic based on experimental findings obtained by various investigations [3,5-12].

Hodgson [8-10], Pells [3], and Shikama [11,12] found permanent electrical degradation in single crystalline alumina due to 1.8 MeV electron, 18 MeV proton and reactor neutron irradiation respectively at temperatures above 600 K and dosages around 10^{-3} dpa (electron and proton radiation) or 10^{2} dpa (reactor neutron radiation) with a simultaneous application of either a direct current electric field or an alternating current electric field from 130 kV/m to 500 kV/m on the sample. The permanent electrical degradation under electron or proton radiation has been postulated to be induced from the aluminum colloid formation inside the materials, because the kinetics of RIED are very similar to that of the colloid formation in some alkali halides under radiation [13] (superlinear increase of conductivity σ versus time with a power of 5 to 6). Results from neutron irradiation, however, show that the increase of conductivity with time has a much lower power value of around 0.5. The formation of aluminum colloids is unlikely to produce the observed permanent electrical degradation considering that aluminum colloids form only after around 10 dpa according to the experimental results by Pells [14,15]. However, results from recent studies by Keternich and Jung [5,6] have suggested that the RIED might be due to surface contamination during irradiation. Optical spectroscopy and electron microscopy analyses from these studies show that carbon deposition is responsible for the electrical degradation observed. In the recent study by Zong [7], attempts were made to search for colloid formation in irradiated alumina, but no such clusters were detected.

3.2 OBJECTIVES

The basic objectives of this investigation are to determine the underlying mechanisms controlling the radiation induced electrical degradation phenomenon in alumina and the role of grain boundaries in the process. This was accomplished by a concerted effort involving a variety of irradiation conditions and sample types.

3.3 EXPERIMENTAL METHODS AND PROCEDURES

The experimental investigation of the radiation-induced conductivity process in alumina was performed by using a variety of controlled radiation sources. These included high energy protons and alpha particles from a 2 MeV light ion accelerator, gamma radiation from a Co^{60} source and x-radiation from an x-ray tube. The experiments were conducted at temperatures up to 823 K. A 2 MeV light ion accelerator (Dynamitron) at Auburn University was used for proton and helium ion irradiations. The average beam current density employed in the irradiations of polycrystalline alumina (both proton and helium) was 800 nA/cm^2 whereas a lower density of 500 nA/cm^2 was used for the proton irradiation of sapphire. A sample holder was designed and fabricated for this study. A schematic of the holder is shown in figure 1. Two types of samples were investigated. The first type was formed by anodizing aluminum to form a thin layer (10 microns thick) of Al_2O_3 on a pure aluminum (99.99%) substrate. The thickness of this layer was controlled electrolytically. The resistance of this thin layer formed in the anodization process was on the order of giga-ohms at room temperature over an area of 0.4 cm^2 in agreement with the expected values for alumina. The second type of samples was single crystalline alpha alumina (sapphire) purchased from the Crystal Systems, Inc. The samples from the above commercial source had a warranty of purity over 99.5%. The purity of the first kind of samples was estimated to be around 95% in atomic percent.

A thin layer (approximately 500 nanometers) of gold was vapor deposited on the alumina surface. The metallic substrate formed another electrode on the other side of the contact. In order to minimize the surface conductivity in the electrical measurements, a guard ring was also formed from gold vapor deposition. The sample was mounted on a ceramic rod and the entire assembly was loaded into the sample

chamber in the 45° right hand leg of the accelerator system. The sample assembly was heated using radiation heating from a tungsten filament in the first series of experiments. Later it was changed to a boron nitride (BN_x) coated graphite heater which provided a better vacuum with much less contamination at high temperatures (>750 K). The sample chamber was evacuated using a diffusion pump to a pressure of 10^{-4} Pa.

The electrical connections were carefully designed and experiments were conducted to ensure the reliability of the resistance measurements during irradiation. Measurements were made to ensure that these readings were not influenced by the ion beam. The magnitude of the beam current was also determined by measuring the potential drop across a shunt resistor from the sample to ground. These readings were compared with periodic measurement of the Faraday cup current and were found to be in good agreement (within 10%).

The effects of gamma radiation were examined using the Co^{60} source (with 1.17 MeV and 1.33 MeV gamma rays with an ionization rate of 0.5 Gy/s) at Auburn University's Nuclear Science Center. A specimen holder was designed and constructed which was capable of heating the specimens to 700 K in a vacuum of 10^{-4} Pa during in-situ irradiations.

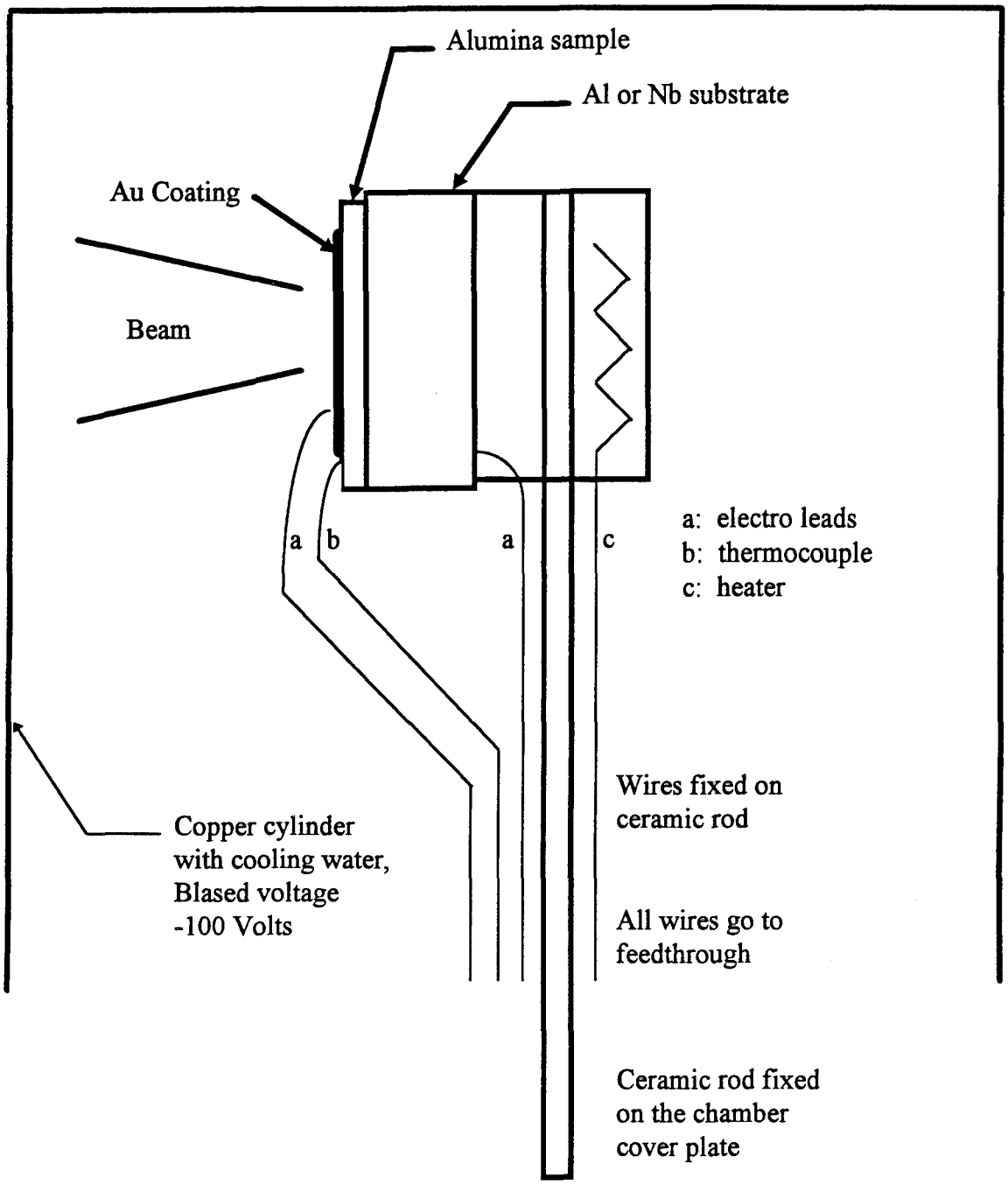

Figure 1. Schematic drawing showing the design of the sample holder for irradiation.

3.4 RESULTS

Figures 2 and 3 show the results obtained from the two experiments on the polycrystalline alumina samples using energetic protons. Both experiments were conducted at 673 K. The average beam current density was 800 nA/cm^2 with a current fluctuation of less than 10% during the length of the experiments. The difference between the two runs was the duration of the experiments (a factor of four). Both samples exhibited an instantaneous increase in conductivity when the beam was turned on. This abrupt change is less apparent in figure 3 due to the difference in the conductivity (y-axis) scale. The digital data values from the early times of figure 3 agree with those from figure 2. This instantaneous or abrupt increase is due to radiation-induced spontaneous conductivity where the high energy ions produce electron hole pairs. A gradual increase in conductivity with irradiation dose followed the initial discrete change. The gradual increase may be a consequence of permanent microstructural change due to irradiation. Upon removal of the ion beam, the insulators recovered a portion of the radiation-induced conductivity. At low doses (figure 2), this recovery corresponds closely to the initial rise indicating that short irradiation does not alter the ion-induced electron hole production process. However, recovery after high dose irradiations (figure 3) is much larger than the initial rise. This suggests that the radiation excitation process has been altered due to a change in the permanent microstructure induced by irradiation.

Analysis of the results obtained indicates that there are two types of radiation-induced conductivities (RIC): recoverable and permanent. In order to separate the dose dependence of the two types of conductivities, the proton beam in the second experiment (figure 3) was periodically interrupted (by inserting the in-line Faraday cup) and the dose-dependent recoverable conductivity was measured as a function of

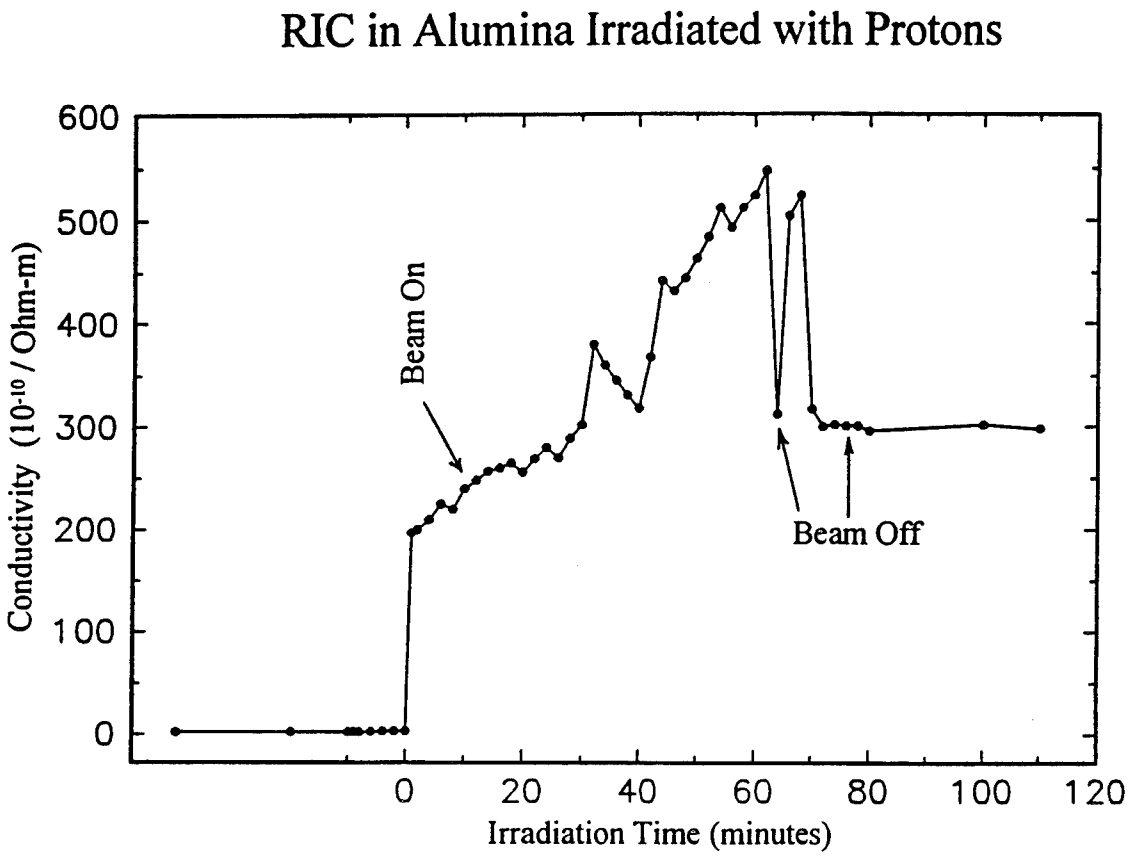

Figure 2. Radiation induced conductance in polycrystalline alumina irradiated with 2 MeV protons at 673 K at an average beam current density of 800 nA/cm^2.

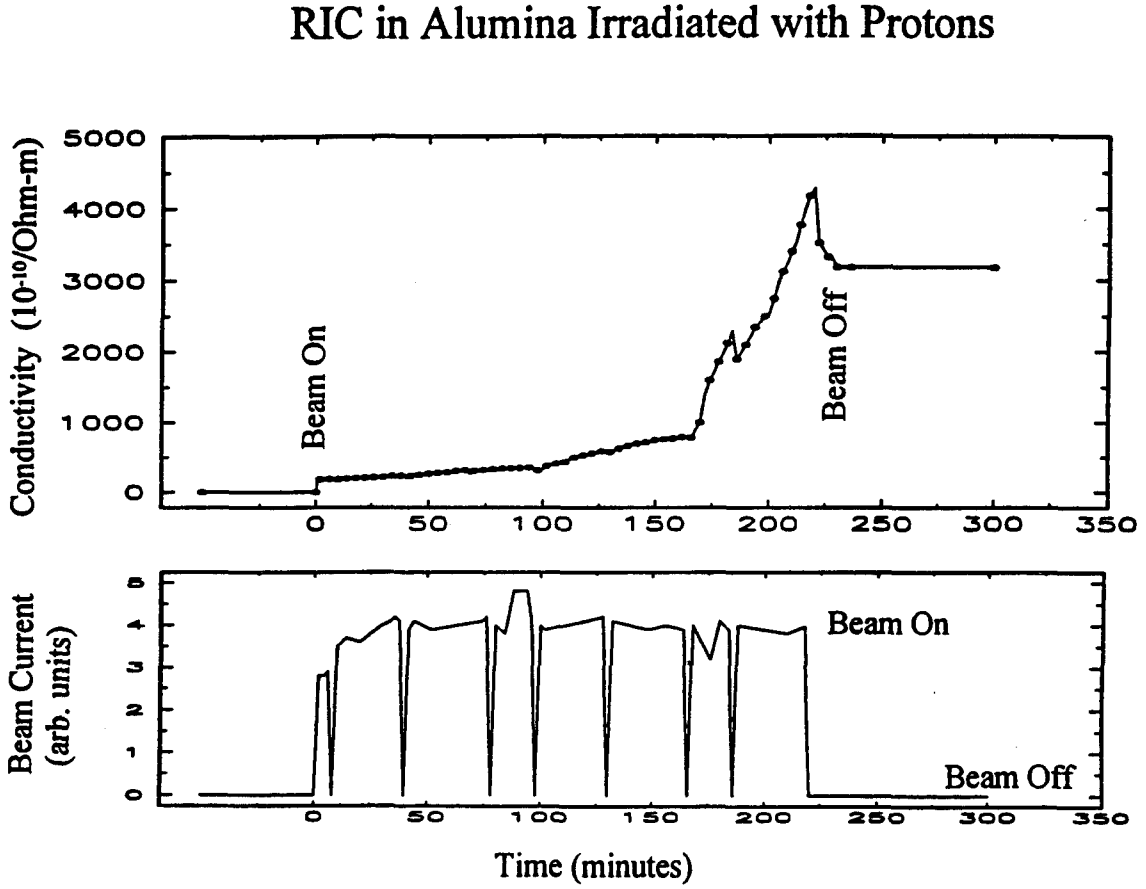

Figure 3. Radiation induced conductance in polycrystalline alumina irradiated with 2 MeV protons at 673 K at an average beam current density of 800 nA/cm^2. Same as figure 2 but irradiated four times as long in duration (also a new sample).

radiation time. The beam current history is illustrated in the bottom of figure 3. The recoverable contribution is related to the decrease in conductivity during the interruption of the beam (the size of the minima in the top graph of figure 3) whereas the permanent conductivity generated by irradiation corresponds to the baseline increase in conductivity when the Faraday cup was inserted. Figure 4 shows the change in these two types of radiation effects as a function of irradiation time. Both RIC (recoverable) and RIED (permanent) were found to increase with dose. The lines represent best fit to the data using a linear regression method.

A similar experiment was conducted on polycrystalline alumina using 2 MeV helium ions. The average beam current density was the same as the proton beam current (800 nA/cm^2). Results are shown in figure 5. A comparison between figures 3 and 5 indicates that helium ions result in significantly higher instantaneous radiation-induced conductivity (evident from the large instantaneous rise in conductivity when the beam was turned on). Similar to the proton case, RIED was observed after an incubation period.

Four irradiations were conducted to examine the effects of proton irradiation on single crystalline alumina (sapphire). Results from one of these experiments are given in figure 6 and is representative of the other sapphire data. This sample was irradiated at a temperature of 800 K and a beam current density of 500 nA/cm^2. The basic response of these samples is significantly different than that observed in polycrystalline alumina. No dramatic permanent electrical degradation was observed in any of sapphire experiments although the irradiation doses in sapphire are over 3 times larger than the critical dose required for the onset of electrical degradation observed in polycrystalline alumina under similar irradiation conditions. During all the sapphire experiments, the beam was periodically interrupted to separate the recoverable component from the permanent one. This is illustrated in figure 6 by the abrupt

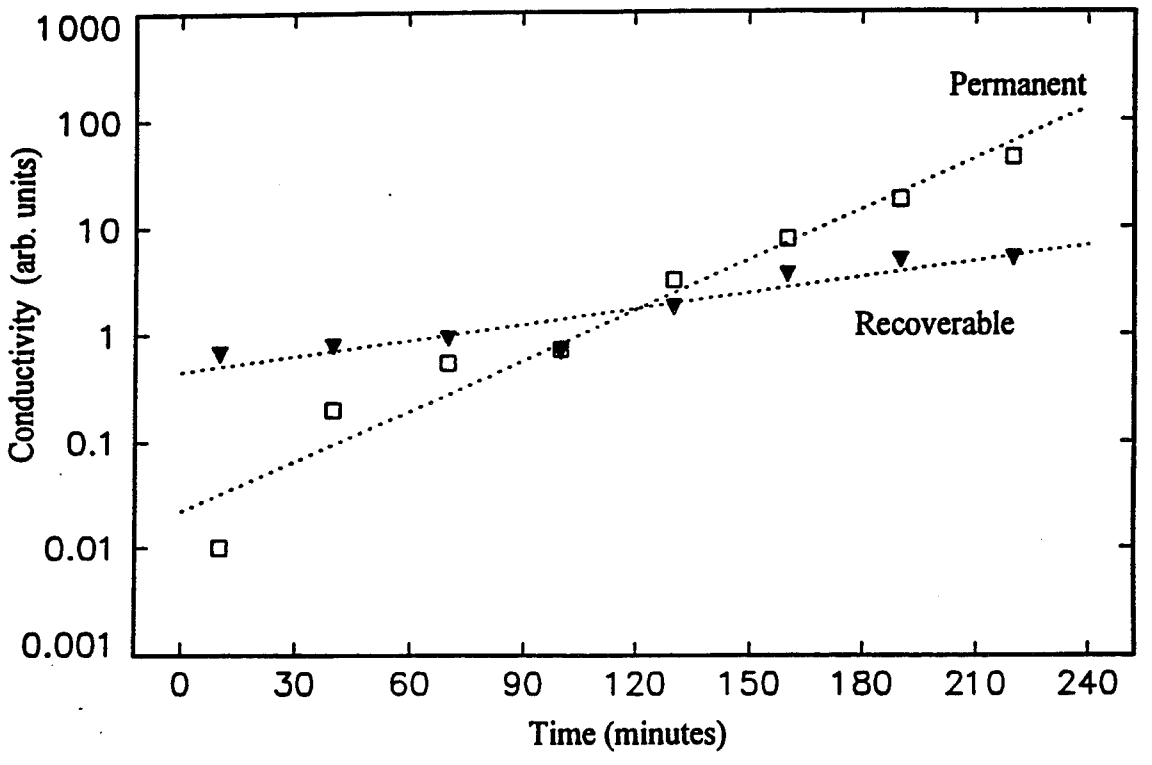

Figure 4. Effects of proton irradiation on recoverable and permanent conductivity. The lines represent best fits to the data using a linear regression method.

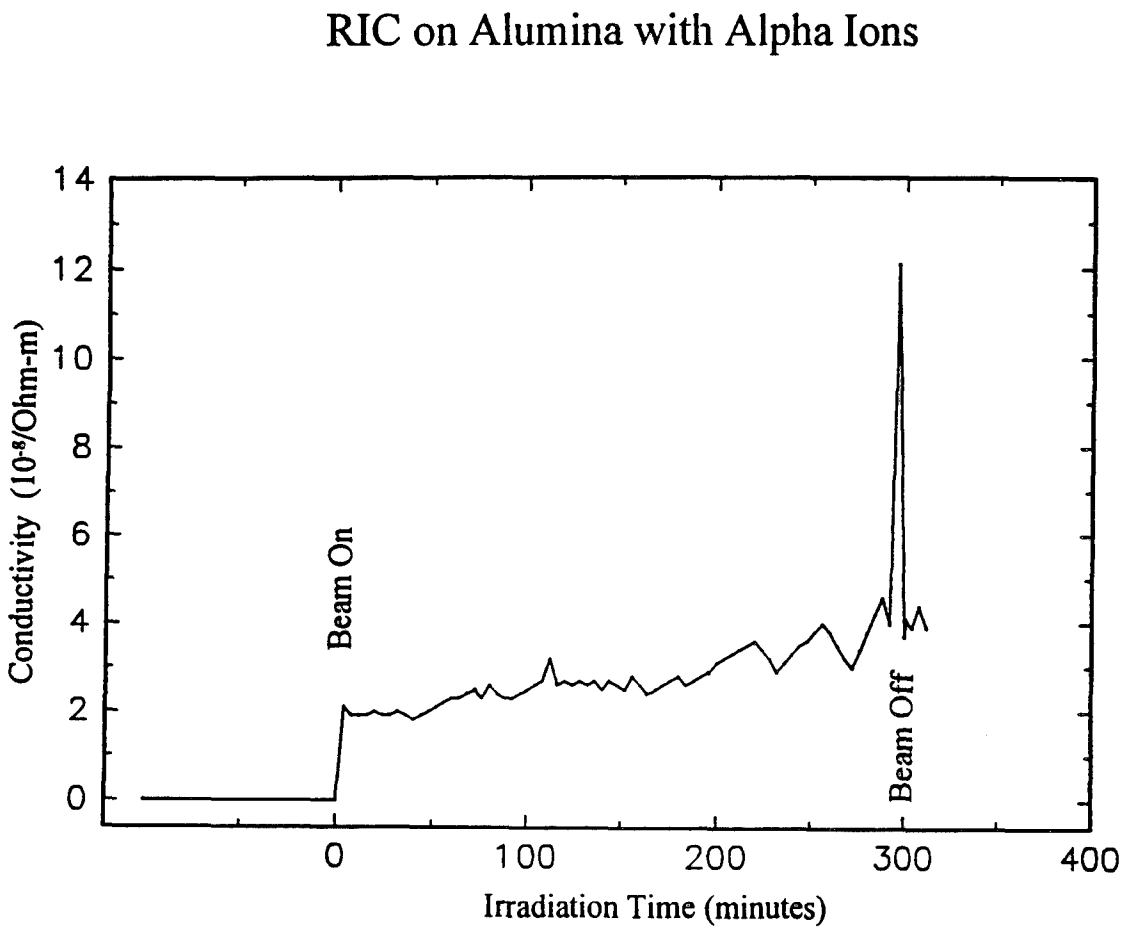

Figure 5. Radiation induced conductivity in polycrystalline alumina irradiated with 2 MeV alpha at 673 K at an average beam current density of 800 nA/cm^2.

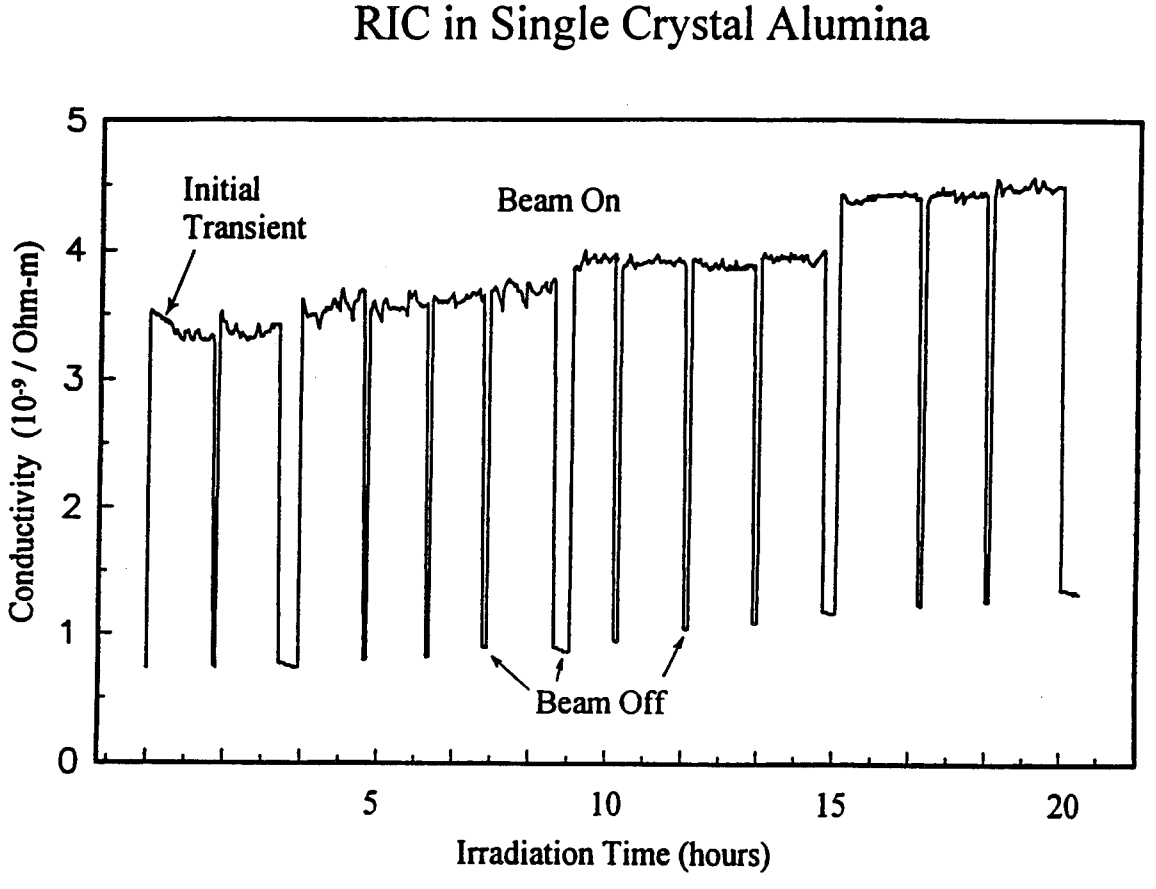

Figure 6. Effects of proton irradiation on the conductivity of sapphire.

decrease in conductivity. These abrupt changes are related to the RIC component whereas the slow increase in the baseline values corresponds to the permanent damage created by irradiation. Some of the beam interruptions occurred at night over long periods of time while the samples were maintained at elevated temperature but with no beam on target. Conductivity of the samples were monitored and results show that no annealing (or recovery) had occurred. The dependence of the base conductivity (permanent conductivity) of sapphire on irradiation for the sample presented in figure 6 is given in figure 7. It increases slowly but remains in the same order of magnitude throughout the experiments.

The effects of gamma irradiation on RIC in sapphire at room temperature are illustrated in figure 8. The conductivity of the material increased abruptly when exposed to the high energy gamma rays at an ionization rate of 0.5 Gy/s. However, the sample resistivity recovered slowly upon further irradiation. No significant degradation in electrical resistivity was observed. In addition, a set of gamma ray irradiation experiments were conducted on polycrystalline alumina and results similar to those observed in gamma irradiated sapphire were obtained, indicating that grain boundaries are not important in radiation induced conductivity, in the case of gamma ray irradiation. Irradiations of polycrystalline alumina were conducted from ambient temperature to 700 K and a summary of the results is shown in figure 9. No temperature dependence of radiation induced conductivity was found.

Results from the proton irradiation on polycrystaline alumina indicate that both recoverable and permanent conductivities increase with irradiation in an exponential manner as illustrated in figure 4. The recoverable conductivity is related to the excitation of electron-hole pairs induced by the ionizing radiation whereas the permanent conductivity is largely governed by the microstructure of the material.

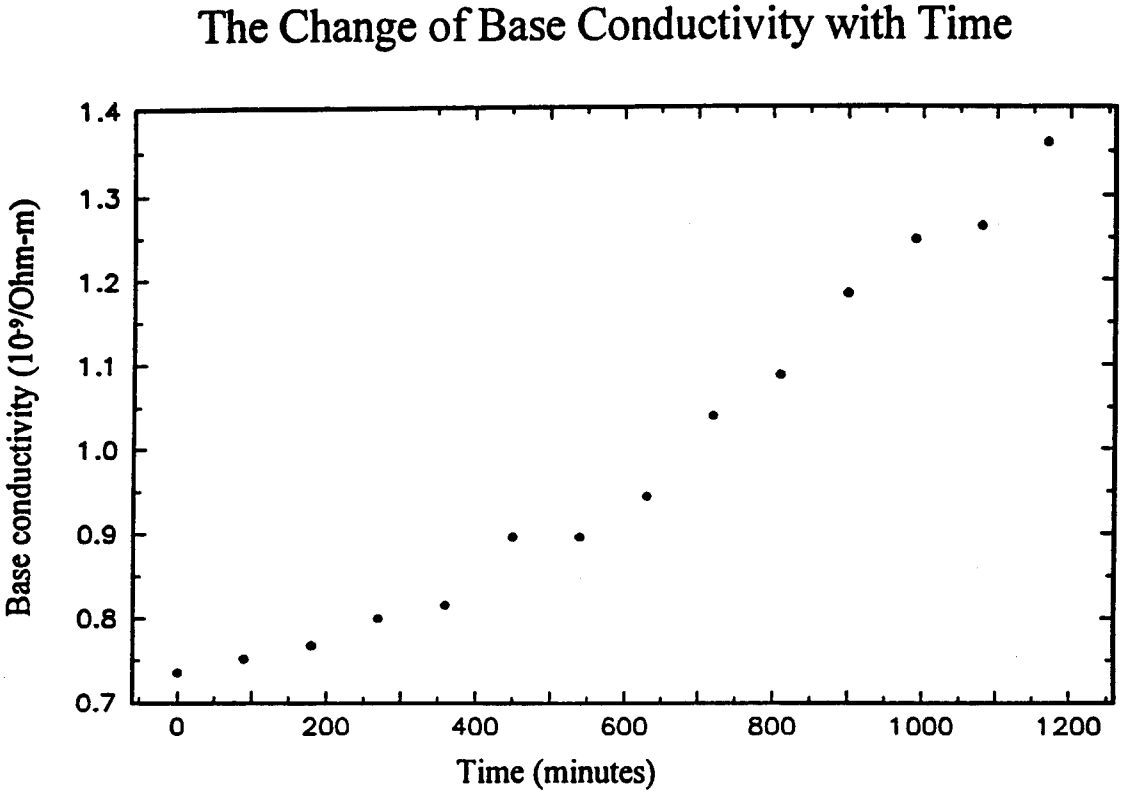

Figure 7. The change of base conductivity of sapphire as a function of irradiation time for the sample shown in figure 6.

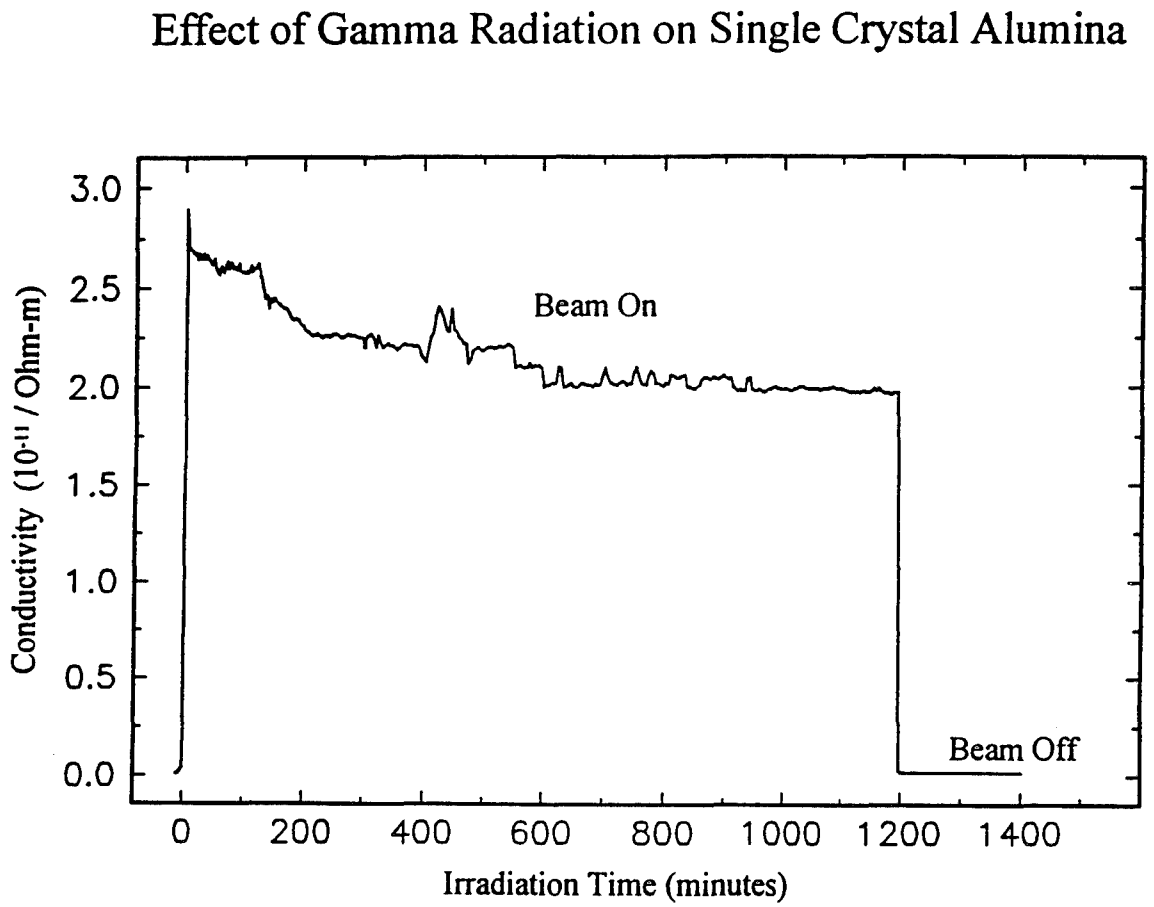

Figure 8. Effect of gamma radiation on the conductivity of sapphire.

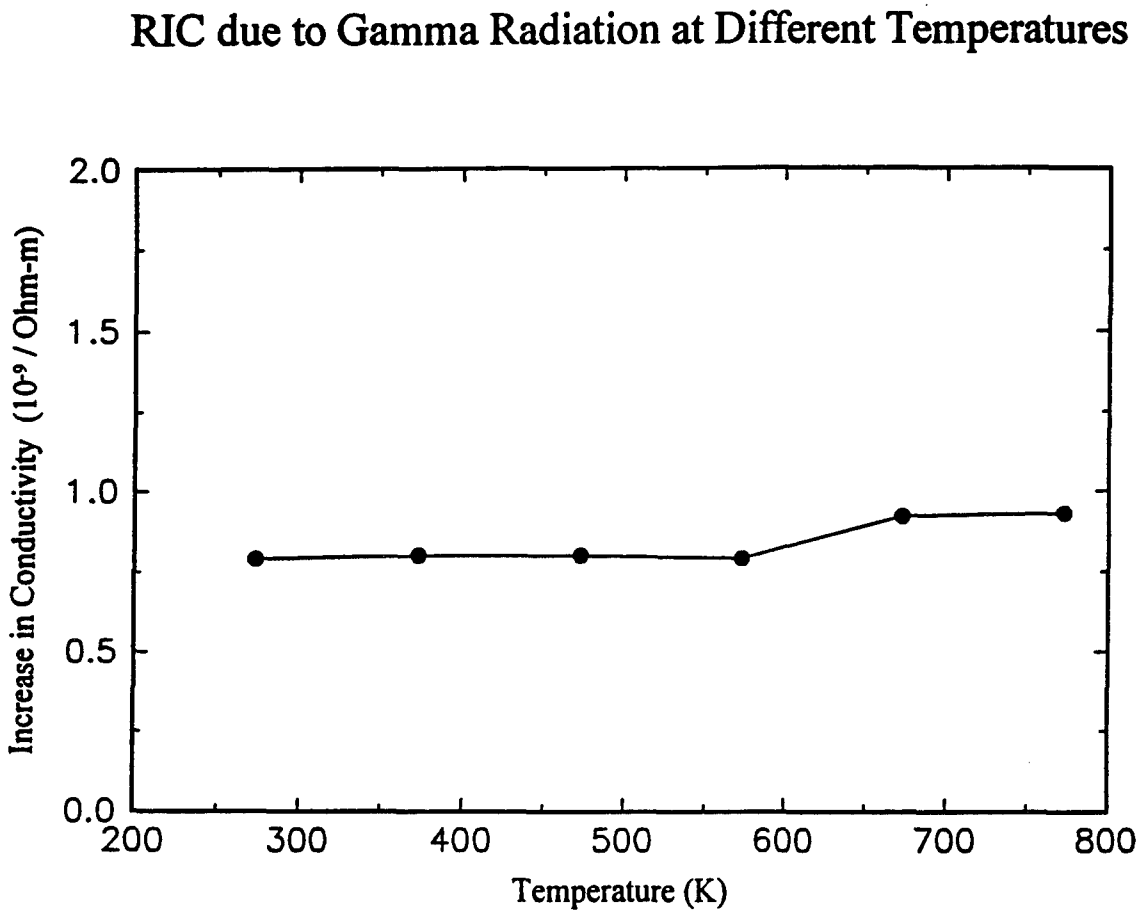

Figure 9. Temperature dependence of gamma induced conductivity in alumina.

However, the former can also be influenced by microstructural changes that affect the electron-hole trapping characteristics of the material. The observed dose dependence in both phenomena suggests that the band structure as well as the microstructure of alumina is changing with irradiation. The mechanism for electrical damage under irradiation is not as well defined. It has been postulated that a radiation enhanced radiolysis process or aluminum colloid formation inside the material may be responsible for the observed increase in conductivity [13]. A comparison of the relevant parameters from different irradiation studies (including neutrons, protons, electrons and gamma) is given in Table 1. This table is by no means exhaustive but does represent a variety of radiation sources and their effects on conductivity. The damage rates and the ionization rates were calculated, by using the computer code TRIM-87, according to the type of irradiation and the intensity. The former is related to the structural damage introduced by the irradiation whereas the latter controls conductivity via valence to conduction band transitions. The parameter $\Delta\sigma$ is the instantaneous increase in conductivity when the irradiation is turned on. Ionization efficiency is defined as the ratio of radiation-induced conductivity ($\Delta\sigma$) to ionization rate and it is a measurement of the effectiveness of a particular ionization mechanism in generating conductivity. Electron and gamma irradiations were found to be most effective in promoting conductivity. Neutrons also possess relatively high ionization efficiency due to the knock-on atoms produced by the neutron irradiation. But it is important to note that neutron irradiations were conducted in a nuclear reactor where high intensity gamma was also present. The ionization process in this case is due in part to such electromagnetic radiation. The variations in the ionization efficiency can be attribution to the difference in the materials (impurity content and level) and radiation spectra. The last column in Table 1 gives the incubation dose (in dpa) when significant radiation induced conductivity was observed under different irradiation

Table 1. Comparison of various radiation effects results.

	Temp (K)	E (kV/m)	Damage Rate (dpa/s)	Ionization Rate (Gy/s)	$\Delta\sigma$ $10^{-10}(\Omega m)^{-1}$	Ionization Efficiency (s/Gy-Ωm)	Incubation Dose (10^{-4} dpa)
Neutron[a]							
On	773	25-500	3.4×10^{-6}	1.4×10^{4}	600	0.04	150
Off	773	25-500	0	150	3	0.02	—
Proton[b] (18MeV)	773	500	4×10^{-7}	5×10^{5}	10,000	0.02	10
Electron[c] (1.8MeV)	773	130	10^{-10}	278	200	0.7	0.1
Proton (2MeV)							
Polycrystal	673	500	3.5×10^{-8}	1.6×10^{5}	200	0.001	2
Sapphire	700-823	500	2.2×10^{-8}	1×10^{5}	40[d]	0.0004	—
Helium (2 MeV)	703	500	2×10^{-7}	2×10^{6}	2000	0.001	20
Co^{60} (γ) Sapphire & Polycrystal	300-753	160	0	0.5	0.2	0.4	—
X-Ray[e]	300	160	0	0.28	0.002	0.006	—

[a]From Shikama 1992
[b]From Pells 1991
[c]From Hodgson 1991
[d]Present study, averaged over four data sets
[e]Unpublished results.

conditions. Alumina irradiated with electrons requires the least incubation dose prior to onset of significant conductivity. No RIED was observed in sapphire under proton irradiation in the present study.

The most significant difference between the results obtained from polycrystalline and single crystal samples is the absence of RIED in the latter. The impurity levels of the two types of samples are low as indicated by their high intrinsic resistivity. The conditions of the two sets of experiments are also almost identical. The single crystals used in this study possess a well aligned orientation with the (1120) plane parallel to the surface. It is possible that channelling that occurs during irradiation of such single crystals might be incompatible with the structure responsible for RIED. A supplementary experiment was conducted where a sapphire sample from the same lot was tilted 10 degrees during irradiation. This misalignment should have resulted in radiation induced degradation if channelling (or any orientation related effects) is responsible for the absence of RIED. However, results obtained from this experiment are identical to that with a well aligned crystal (such as that shown in figure 6) indicating that crystallographic orientation is not important. This leads to the conclusion that the observed RIED in polycrystalline alumina is attributed to the presence of grain boundaries. In all the experiments conducted in this study, a thin layer of gold was deposited on the surface of the sample prior to irradiation. It is possible that radiation enhanced diffusion has occurred during irradiation of the polycrystalline alumina through the grain boundaries. The absence of grain boundaries in sapphire would have prevented such diffusion in agreement with the observed results. A series of experiments were conducted to determine the gold distributions in these materials using the Rutherford backscattering (RBS) technique [16]. The accelerator employed for the irradiation experiments was used for this purpose with a 2 MeV helium ion beam for profiling at a scattering angle of 170 degrees. Figure 10 shows the RBS spectrum obtained for an alumina sample prior to

irradiation and the profile for sapphire is identical. The gold contribution to the profile was sharp indicating that a discrete layer was deposited with no diffusion in both types of starting materials. Figures 11 and 12 show the RBS profiles for sapphire and polycrystalline alumina after irradiation where the resistivity of sapphire is preserved whereas the polycrystalline materials has degraded significantly. The broadening of the gold peak in figure 12 indicates that significant inward diffusion of gold has occurred in polycrystalline alumina. No such broadening was detected in figure 11. A comparison of the two profiles leads to the conclusion that grain boundary diffusion due to irradiation is responsible for the observed difference between the two materials. A final RBS experiment was carried out to identify the thermal contribution to the grain boundary diffusion. A polycrystalline sample was deposited with a thin layer of gold and annealed at 800 K for 24 hours without irradiation. Subsequent RBS analysis shows that the deposited gold layer remains discrete. This indicates that radiation is critical to the rapid diffusion of gold through the grain boundaries leading to dramatic changes in the conductivity of the polycrystalline materials.

Experimental results obtained in the present study regarding the higher susceptibility of polycrystalline alumina than sapphire to RIED are contrary to the observation of Hodgson where the degradation process was found to be faster in sapphire [17]. The earlier work is likely based on electron irradiation of thicker samples (not specifically stated in the paper) with different experimental arrangements, including applied field and measurement conditions. It is possible that the thicker specimens used in Hodgson's study (millimeter instead of micrometer) would have significantly increased the dosage required for radiation enhanced grain boundary diffusion to occur through the thickness. The electrical degradation observed in electron irradiated sapphire may have been a surface contamination effect.

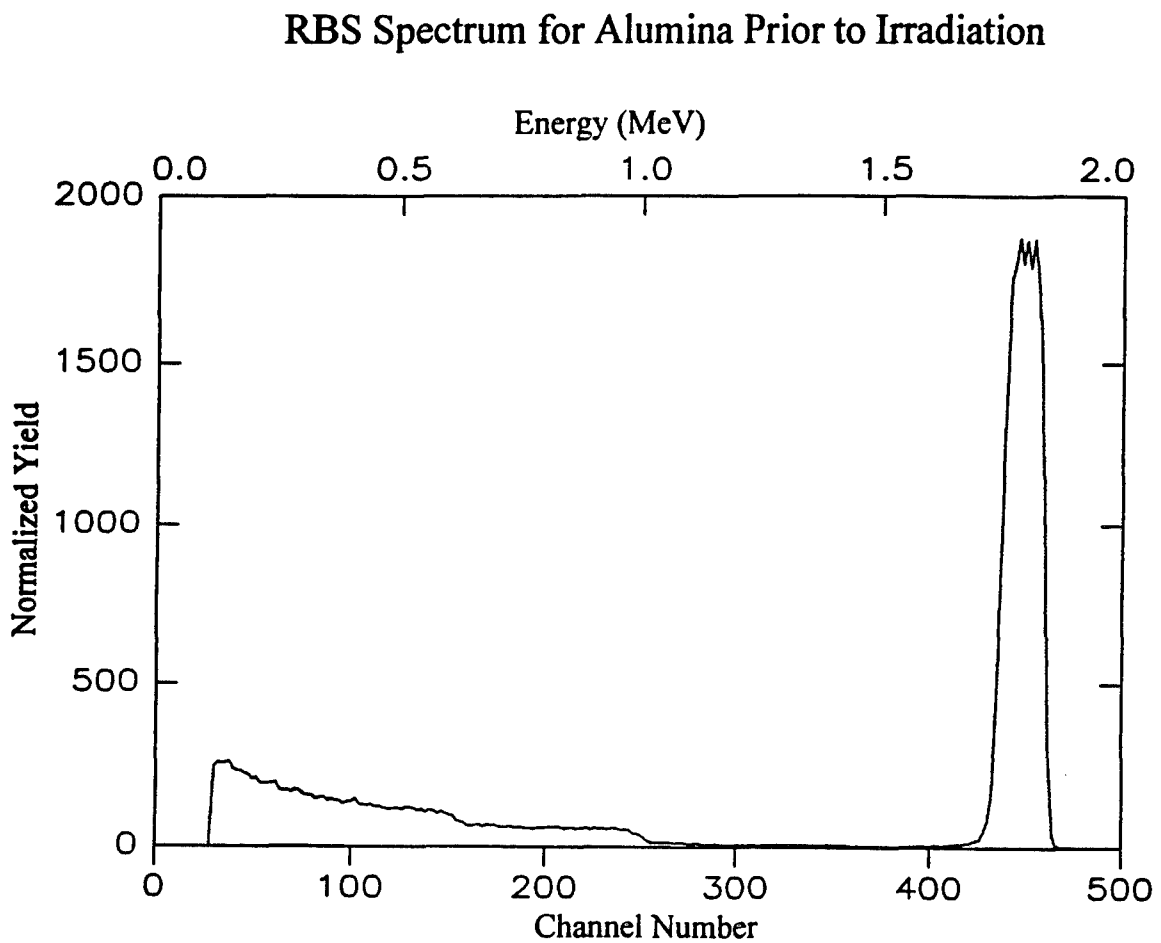

Figure 10. RBS spectrum obtained for alumina prior to irradiation.

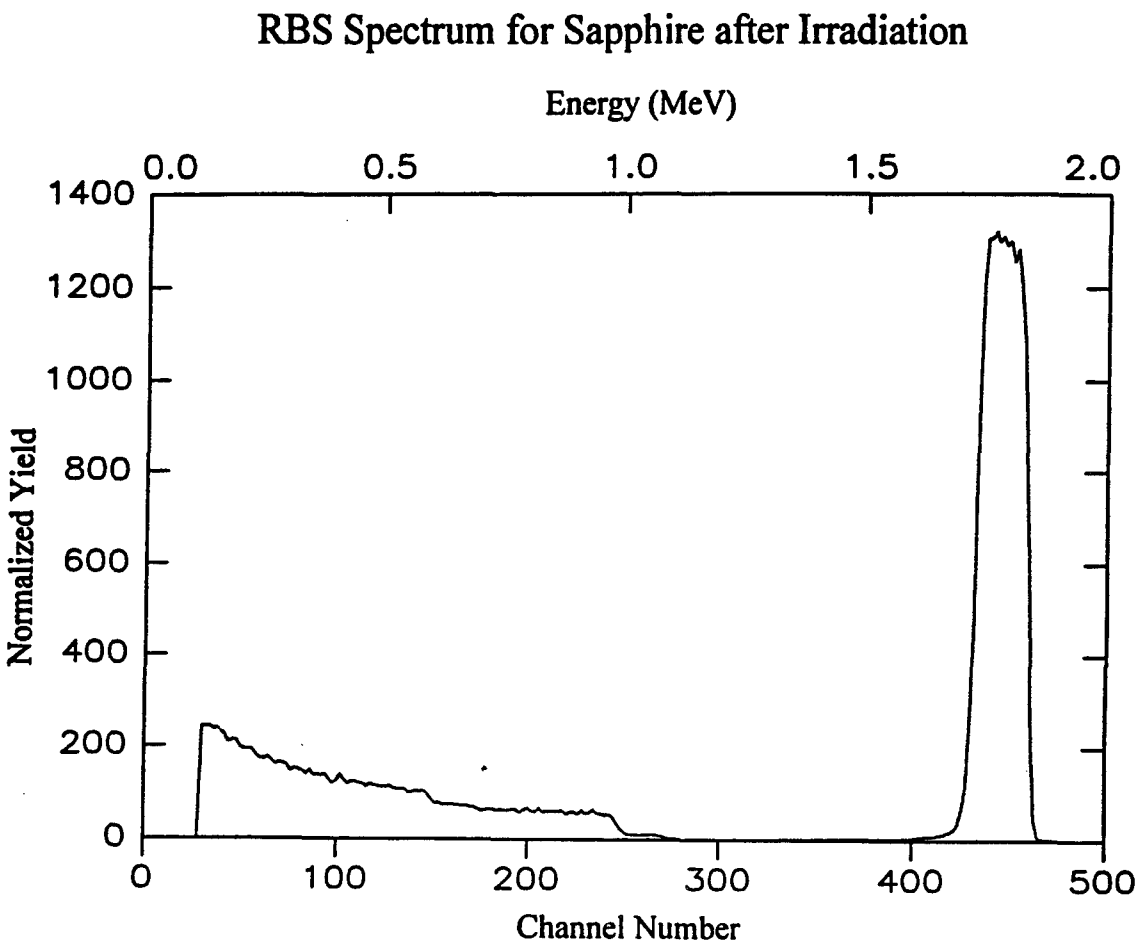

Figure 11. RBS spectrum obtained for sapphire after irradiation of 2 MeV protons at 800 K at an average beam current density of 500 nA/cm^2 for 20 hrs.

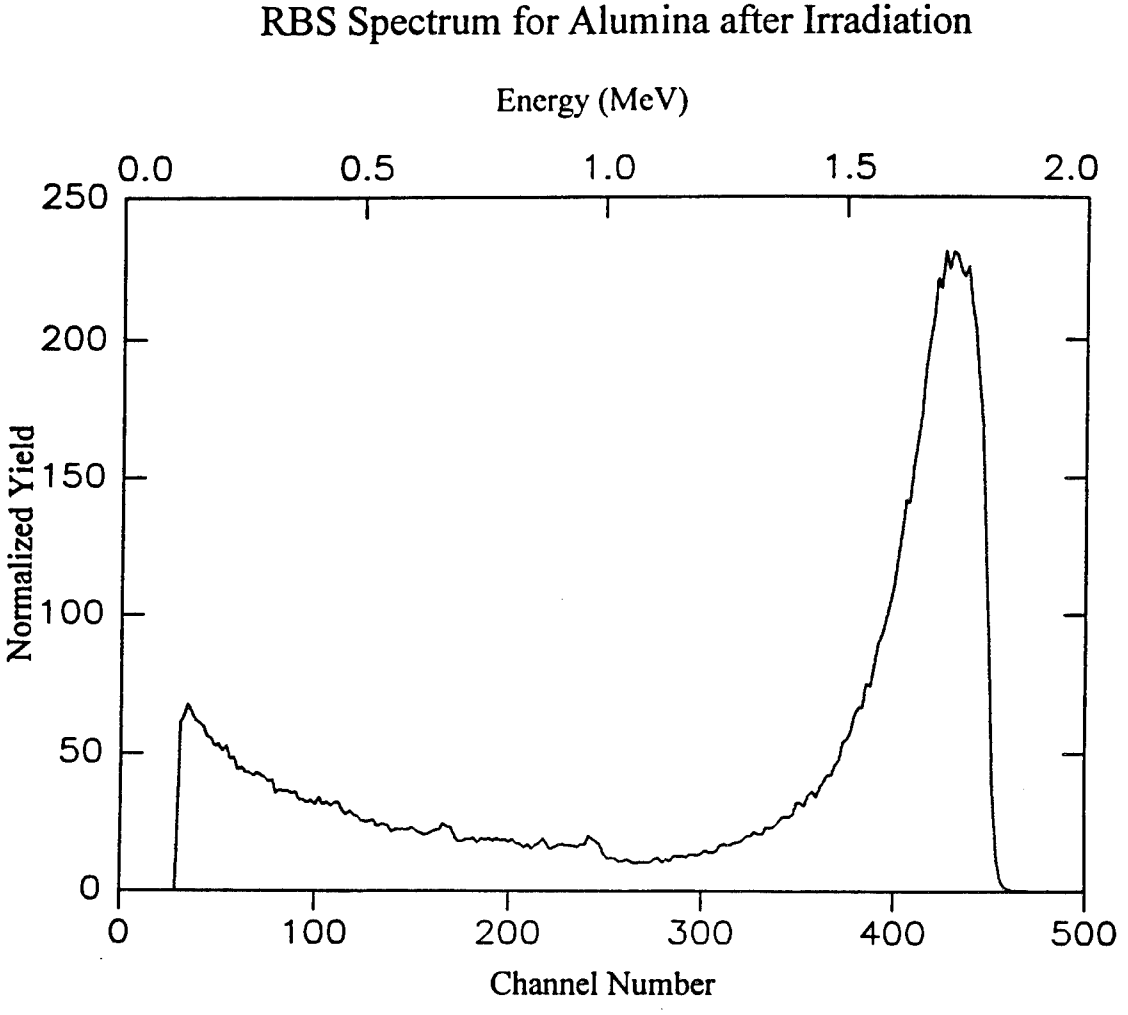

Figure 12. Same as figure 10 but for polycrystalline alumina, showing extensive inward diffusion of the deposited gold layer.

Electrical conductivity was found to decrease after the initial jump for sapphire during gamma irradiation (see figure 8). The same behavior, but to a lesser extent was observed during proton irradiation as indicated by the arrow labeled as initial transient in figure 6. Such a transient was not observed in any of the polycrystalline sample. The gradual decrease in conductivity with irradiation after the initial rise has also been observed by Farnum [18] where sapphire was irradiation with 3 MeV protons at 300 and 373 K. These experimental results indicate that the free electron concentration is decreasing after the initial jump induced by both proton and gamma radiation. Electron traps must have been introduced in these radiation processes to absorb those electrons excited by radiation. If the microstructure of the material remains unaffected by irradiation, the conductivity should approach a steady state condition without such a transient. This transient is most likely a result of the generation of traps due to the irradiation. The irradiation carried out by Farnum [18] is at lower temperatures than those conducted in the present study (700 to 800 K). At elevated temperatures, thermal annealing of the radiation induced carrier traps occurs more rapidly than at ambient temperature resulting in a smaller transient observed in the present study of proton irradiation of sapphire. To examine the role of the irradiation environment that could contribute to this transient, an experiment was conducted under similar conditions as those used in the sample of figure 6 but with a lower vacuum level. In all the experiments described thus far, the samples were heated using a BN heater which provided a clean irradiation environment. In a separate experiment, a sapphire sample was heated to 700 K using a radiative method which resulted in a more contaminated environment (10^{-3} Pa instead of 10^{4} Pa with the BN heater). The excess residual gas produced by the radiative heater resulted in a larger transient in the initial stage. This is attributed to the introduction of artifacts due to the contamination in the conductivity measurement as suggested by other investigators [5,6]. The transient effect observed under the contaminated environment was very similar to that observed by Farnum at room temperature but with a good vacuum. This suggests that the

accumulation of carrier trapping sites at room temperature and the excess generation rate of similar sites due to surface contamination may have similar effects on the transient phenomenon and the interpretation of the transient must be treated with care.

3.5 CONCLUSIONS

Different kinds of radiation sources have been used to investigate the radiation effects in alumina. Both recoverable and permanent radiation-induced conductivities were observed in proton and helium ion radiated polycrystalline alumina, while mainly recoverable conductivity was detected in sapphire. The recoverable conductivity is related to the excitation and associated trapping and detrapping of electron-hole pairs induced by ionization whereas the permanent conductivity is governed by the microstructure of the materials. Radiation induced electrical degradation was observed in the polycrystalline specimens but not in single crystal sapphire after similar irradiations. Results from RBS analyses of the irradiated and control samples indicate that radiation enhanced grain boundary diffusion in the polycrystalline structure is responsible for the observed electrical degradation in alumina. The transient radiation induced conductivity observed in sapphire during proton and gamma irradiations is affected by the free carrier generation rate and the production of defect trapping sites due to irradiation.

4.0 GROWTH OF REFRACTORY ALLOY SINGLE CRYSTALS

Many advanced energy systems require components that can sustain high temperature operation with minimal deformation over long periods of time. For example, fuel elements used in thermionic systems for direct thermal to electric power conversion must be able to withstand high temperatures (1800 K) over lifetimes in excess of seven years [19]. The maximum steady state creep rate of the thermionic fuel element must be maintained below $4.5 \times 10^{-11}\ s^{-1}$ in order not to exceed 1 percent creep deformation at the end of life. Only tungsten-based and molybdenum-based alloys appear to be able to satisfy such stringent requirements. Single crystalline materials have been proposed for many high temperature engineering components.

4.1 BACKGROUND

The attributes of single crystals, compared to their polycrystalline counterparts, include more stable microstructures, lower creep rates, better compatibility with nuclear fuels and lower diffusion penetrability [20]. Even with the high creep resistance of single crystals, premature creep failure remains one of the critical issues in these types of materials. Better creep resistant materials are needed to meet the design specifications for advanced engineering systems. Since atomic size mismatch and alloy content have significant effects on creep rates, hafnium and niobium have been considered as the best strengthening agents for molybdenum due to their large atomic size mismatch and high solubility. Binary alloys of molybdenum with up to 11% Nb or up to 15% Hf were examined in this study. All compositions quoted in this report are in atomic percent.

4.2 OBJECTIVES

The technical goals of this study are to determine the feasibility of growing refractory alloy single crystals of molybdenum and the conditions with which optimum crystals can be processed. The effects of alloy composition (solute type and concentration), dissolved gases, scan rate and scan conditions were to be correlated with crystal quality.

4.3 EXPERIMENTAL METHODS AND PROCEDURES

Electron beam zone melting is a well-known method for preparation of refractory metal rod and tube [21-26]. The melting ability of the system depends on the characteristics of both the power supply and the electron beam gun designs. An emission current control system was utilized in the power supply in order to minimize the effects of the ionization of metal gases evolved from the molten zone. A pair of focussing plates were used to obtain a thin molten region. On the other hand, the quality of as-grown single crystals depends on the composition of raw materials, the gas content in the initial materials, the times of zone scan and the final scan rate. Since the alloys developed in this study were not commercially available, all alloy rods were prepared by a powder metallurgy method. This research investigated the effects of both scan rate and scan number on the single crystal formation and solute distribution.

The raw materials with their nominal compositions indicated in Table 2 were compacted into solid rods by a powder metallurgy method. Appropriate portions of the powder constituents were mixed in a jar mill and then cold pressed into green pellets inside a stainless steel mold. These pellets were then sintered in a vacuum furnace (10^{-4} Pa) at 1873 K for sixteen hours. The annealed pellets were 95% dense.

The pellets were stacked to form a 70 mm-long rod and loaded into the growth furnace. The chamber of the growth facility was evacuated by a high capacity cryopump and maintained at a base vacuum of 10^{-6} Pa prior to heating. The maximum pressure of the chamber was 10^{-4} Pa during the growth process due to out-gassing of the rods and the wall of the hot chamber. Although the chamber wall was actively cooled by water, radiative heating from the specimen at the center of the chamber resulted in an equilibrium chamber wall temperature of about 350 K. The heat source for the zone melting of the specimen was electron beam bombardment from a 20 kV DC power supply with a current capacity of 1 A. The rod was driven along its axis using a servo motor and a set of threaded rods converting the circular motor motion into linear movement. The electron beam gun was held stationary. Out-gassing of the dissolved gases and evaporation of the metal vapor from the molten zone caused ionization problems leading to power output fluctuations, and frequently resulted in system shutdown. A constant emission current regulation was incorporated to compensate such current fluctuations. A schematic of the electron beam gun used in this study is shown in figure 13. The use of two focussing plates provided a thin molten zone needed for quality crystal growth. The filament was set near the lower focussing plate to provide a path for the metal vapor evaporated from the molten zone thereby minimizing the discharge problem.

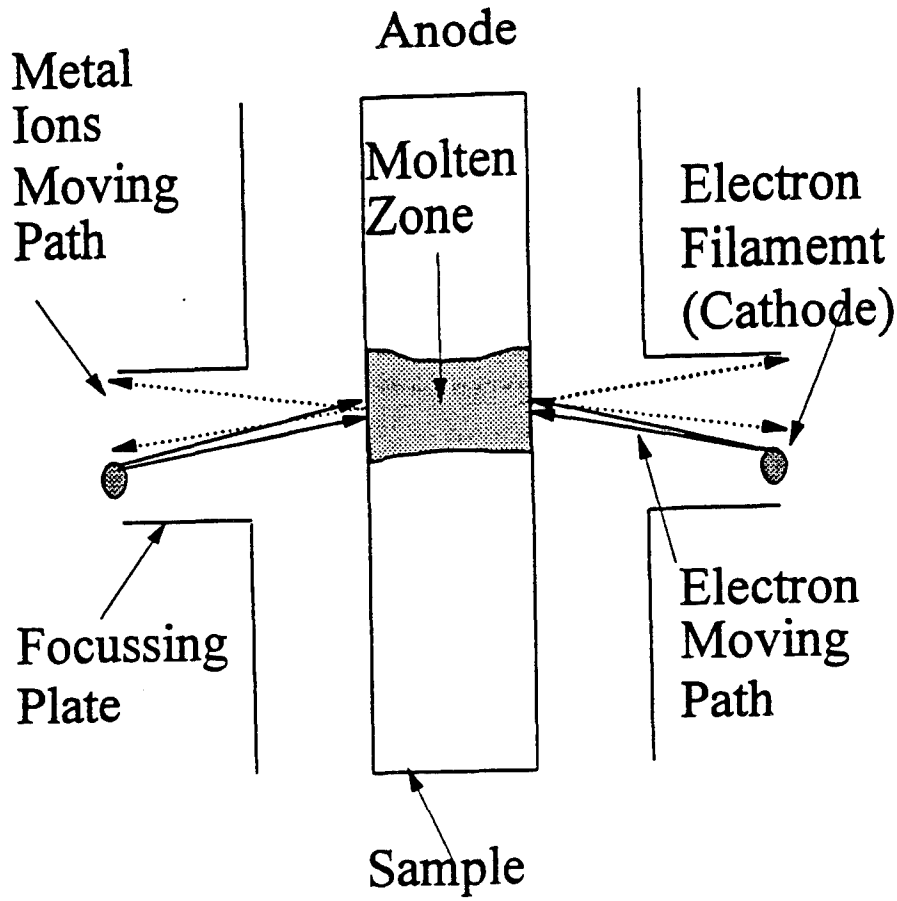

Figure 13. Schematic drawing showing the design of the electron beam gun used in this study.

Table 2. Procedures for the preparation of alloys and their microstructure.

Nominal Composition (Atomic Percent)	**Melting Procedure**	**Microstructure of the As-Grown Alloys** (Cross Section near the End)
Mo-2%Nb	Triple scan: all at 55 mm/h	Single crystal
Mo-11%Nb	Triple scan: all at 55 mm/h	Single crystal
Mo-018%Hf-0.43%C	Triple scan: all at 55 mm/h	Single crystal
Mo-0.8%Hf-0.43%C	Triple scan: all at 55 mm/h	Single crystal
Mo-1%Hf	Double scan: both at 55 mm/h	Single crystal
Mo-2%Hf	Double scan: both at 55 mm/h	Polycrystal
	Triple scan: first two at 55 mm/h, third at 22 mm/h	Polycrystal
	Same as above but with fourth scan at 11 mm/h	Single crystal
Mo-2.75%Hf	Double scan: both at 22 mm/h	Single crystal
Mo-3.7%Hf-1%C	Double scan: both at 11 mm/h	Single crystal
Mo-10%Hf-2%C	Triple scan: all at 11 mm/h	Polycrystal (eutectic-like structure)
Mo-15%Hf	Triple scan: all at 11 mm/h	Polycrystal

Solute segregation was present along the scan direction due to the zone refining effect. Reduction of this solute segregation has been accomplished by choosing fast scan rates or stirring the molten zone by rotating the two segments of rod in opposite directions [27]. Since rotating the rod is complicated and cannot be easily achieved in a high voltage environment, the fast scan rate approach was chosen in this study. In addition, since the raw materials had approximately 5% porosity, out-gassing of the samples was a serious problem. The zone scan speed had to be kept sufficiently low to facilitate proper degassing of the samples during melting and to maintain a stable liquid-solid interface. Multiple zone passes were needed in order to further minimize the out-gassing problem in order to obtain quality single crystals. However, the number of scans cannot be too large and the scan speed cannot be too low in order to minimize material loss due to liquid phase evaporation. Therefore, optimum procedures depending on alloy compositions had to be determined experimentally. The details of the experimental procedures used for processing each alloy are given in Table 2.

For microstructural analysis, a thin disk was cut from the region of the sample near the end. The sample was electrically polished and etched. An electro-etching solution of 20% H_2SO_4 and 80% methanol was used. The electrode was graphite and a voltage of 15 V was used for polishing and a lower voltage of 1.5 V for etching. The times for polishing and etching were 180 seconds and 30 seconds, respectively. The microstructure of the samples was then analyzed using optical microscopy and scanning electron microscopy. Laue back diffraction patterns of the samples were obtained under the conditions of 30 kV, 30 mA and with a 3 cm sample-film stand-off distance. The identification of the formation of single crystals was accomplished by confirming the lack of high angle grain boundaries and Laue diffraction patterns obtained at several locations along the scan direction. The surface morphology of some of the as-grown crystals is shown in figures 14 to 16. Typical microstructure

and the Laue patterns are provided in figures 17 and 18.

The distribution of Hf in the crystals was examined using energy dispersive analysis on the scanning electron microscope. Samples from the Mo-3.71%Hf-1%C, Mo-10%Hf-2%C and Mo-15%Hf crystals were analyzed along the longitudinal direction. The surface analyzed was electrically polished.

4.4 RESULTS

The temperature difference between the solidus and the liquidus lines is a critical parameter for the growth characteristics of single crystals. When the temperature difference exceeds a critical value, which depends on the composition of alloys, diffusion rates of the solutes, the scan rate and the diameter of the rod [28], and constitutional supercooling in the advance of the solid-liquid interface can occur. High solute contents and high scan rates tend to lead to constitutional supercooling and prevent the formation of single crystals. This temperature difference (related to the two phase liquid plus solid region in the binary phase diagram) is a function of composition and is given in figure 19 for Mo-Hf and Mo-Nb. The vertical width of the two phase region in the phase diagram is significantly smaller in the Mo-Nb system compared to that in Mo-Hf, indicating that single crystals could be formed easier in the former type of alloys. Furthermore, the Mo-Nb system exhibits complete solid solubility at all concentrations whereas numerous intermetallic phases are present in Mo-Hf. The as-grown crystals were always polycrystalline in nature after the first scan because of the porosity of the raw materials and incomplete out-gassing. At least two scans were necessary. It was found that for Mo alloys with up to 11% Nb, a high triple scan rate of 55 mm/hour (all these scans were at the same rate) was capable of producing satisfactory single crystals. Mo-1%Hf, Mo-2.75%Hf and

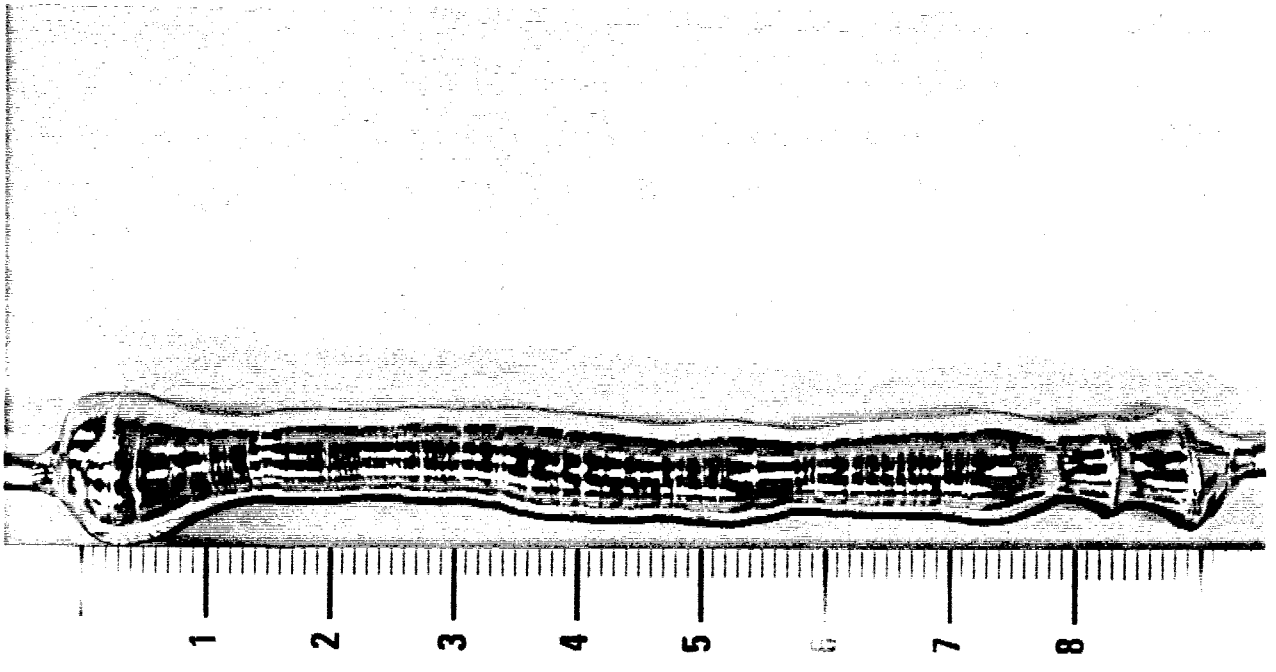

Figure 14. The surface morphology of an as-grown Mo-11%Nb single crystal (scale is centimeter). The smaller rods at the two ends are the support rods.

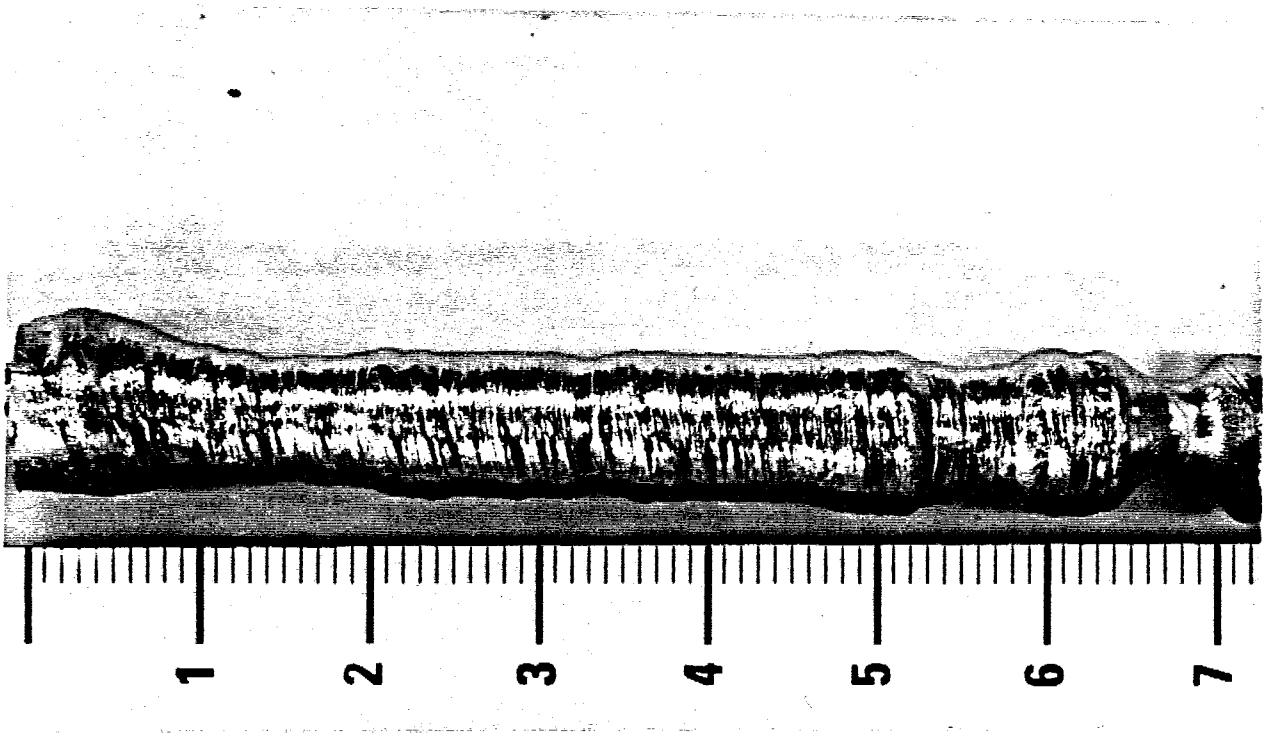

Figure 15. The surface morphology of an as-grown polycrystalline Mo-2%Hf (scale is centimeter).

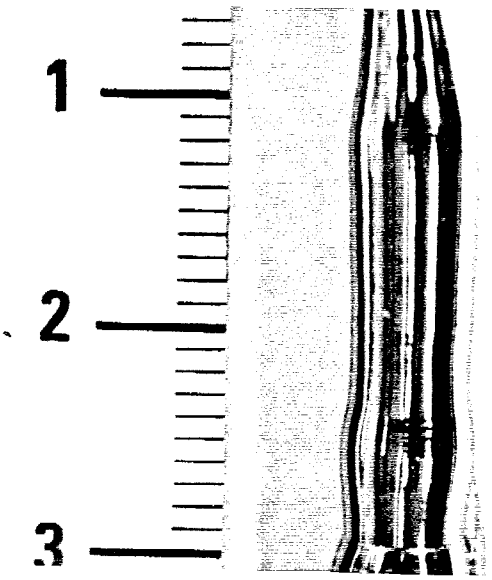

Figure 16. The surface morphology of an as-grown Mo-2%Hf single crystal (scale is centimeter).

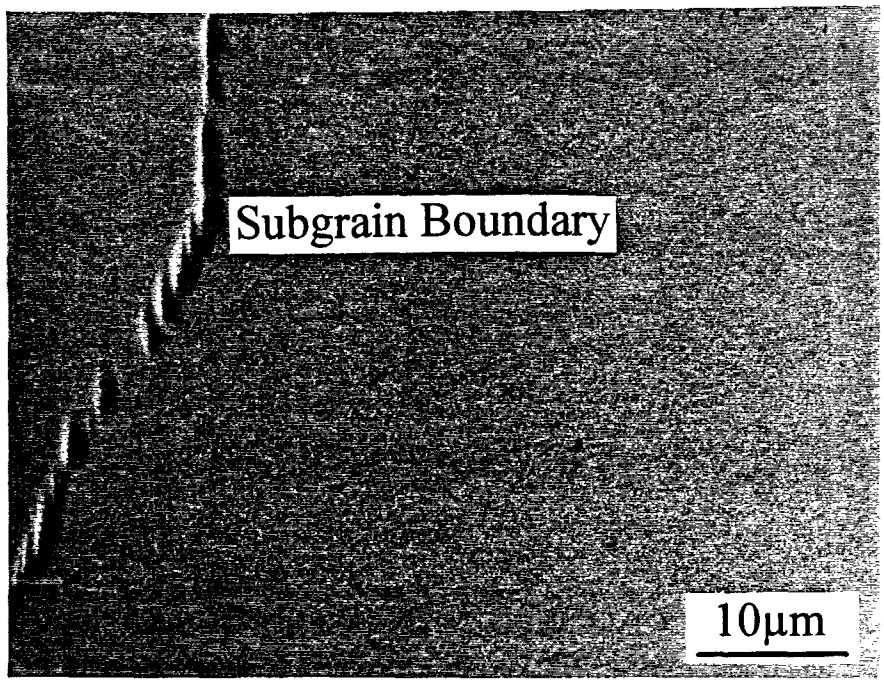

Figure 17. Typical microstructure on the cross section of a Mo-2%Hf single crystal.

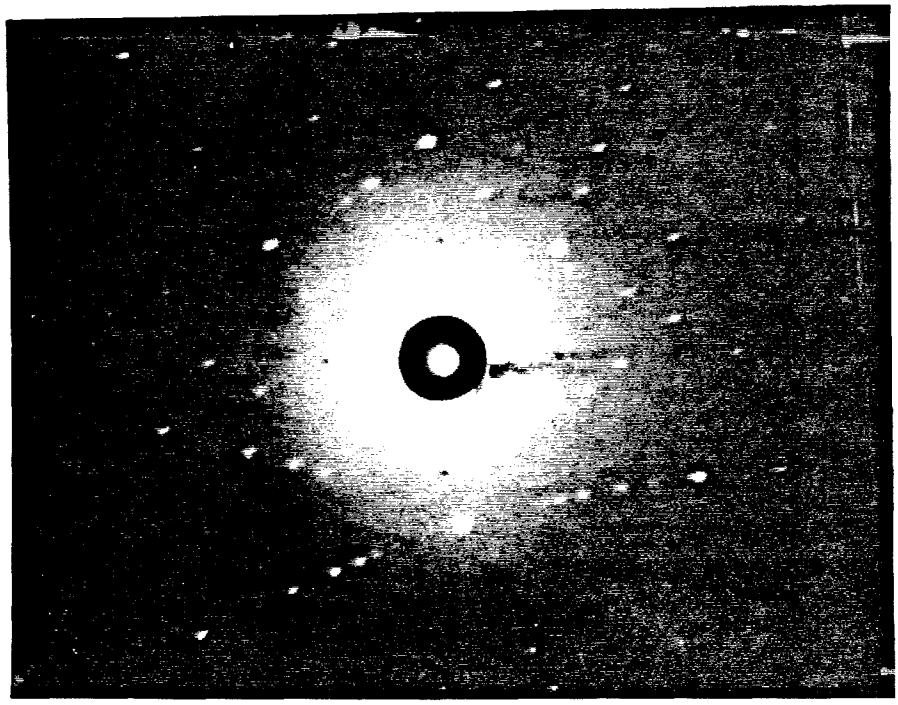

Figure 18. Laue pattern taken from the cross section of a Mo-2%Hf single crystal.

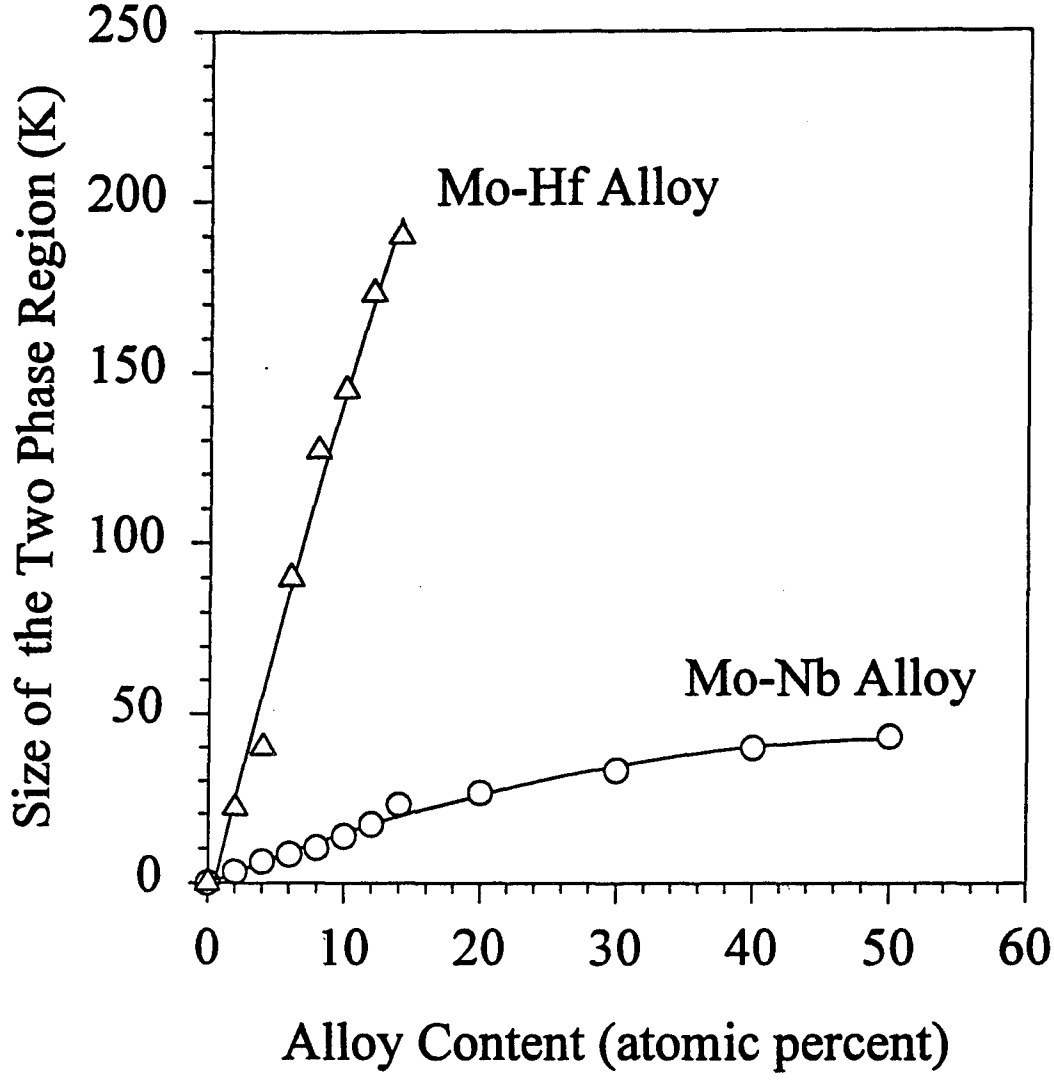

Figure 19. Temperature difference between the liquidus and solidus lines of the Mo-Nb and Mo-Hf systems.

Mo-3.71%Hf-1%C could be grown into single crystals after two scans. The scan rates for the three above alloys were 55 mm/hour, 22 mm/hour and 11 mm/hour. The critical scan rate for single crystal formation decreased with increasing Hf content in the Mo-based alloys investigated. The critical scan rates for Mo-Hf alloys are summarized in figure 20. The maximum scan rate for the formation of Mo-5%Hf single crystal was estimated at 2 mm/hour. The scan rate of any particular alloy must be slower than the maximum rate which is a function of composition, in accordance with the prediction of the supercool model. For instance, attempts made on Mo alloys with 10 to 15%Hf at a scan rate of 11 mm/hour were unsuccessful, still resulting in polycrystalline alloys.

No compositional segregation (or variation) was found in any of the as-grown crystals in the radial direction. However, solute concentration variations were observed along the scan direction. The composition profiles in the crystals are shown in figures 21 to 24. Figures 21 and 22 indicate that the scan rate higher than 11 mm/hour would be appropriate for the first scan. Figures 22 to 24 indicate that the degree of solute segregation can be reduced to an acceptable level by choosing scan rates higher than 22 mm/hour when processing the Mo-Hf single crystals. The degree of segregation was expected to be significantly lower in Mo-Nb alloys compared to Mo-Hf materials because of the relatively small composition difference in the two phase (liquid plus solid) region in the Mo-Nb system. This trend was observed in the experimental study.

No high angle grain boundaries were found in the single crystals. Although subgrain boundaries in the form of low angle tilt boundaries were present in certain crystals, the consistency of the Laue patterns along the entire length of each crystal indicated that the orientation difference of these sub-boundaries was small. The formation of these

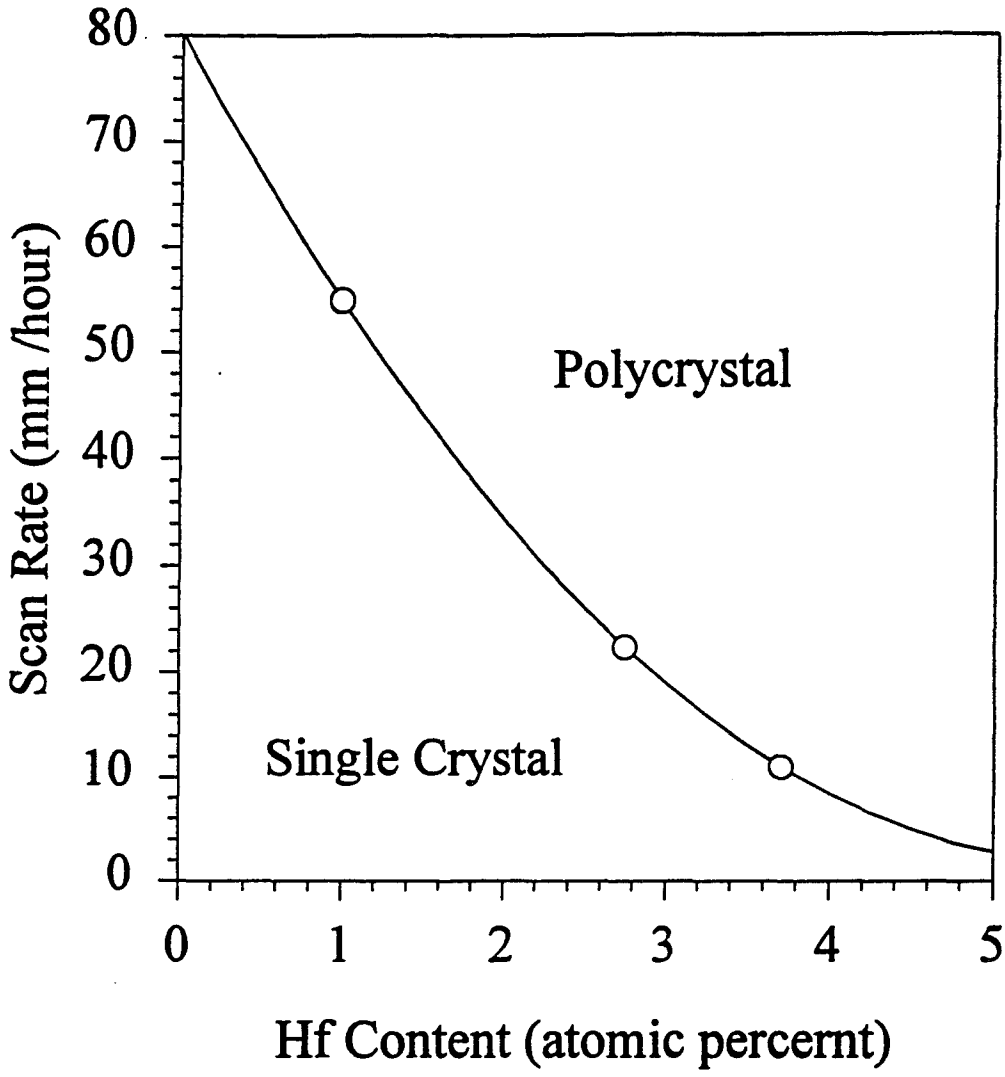

Figure 20. Experimentally determined maximum scan rate (dual scan) as a function of hafnium content required for forming Mo-Hf alloy single crystals.

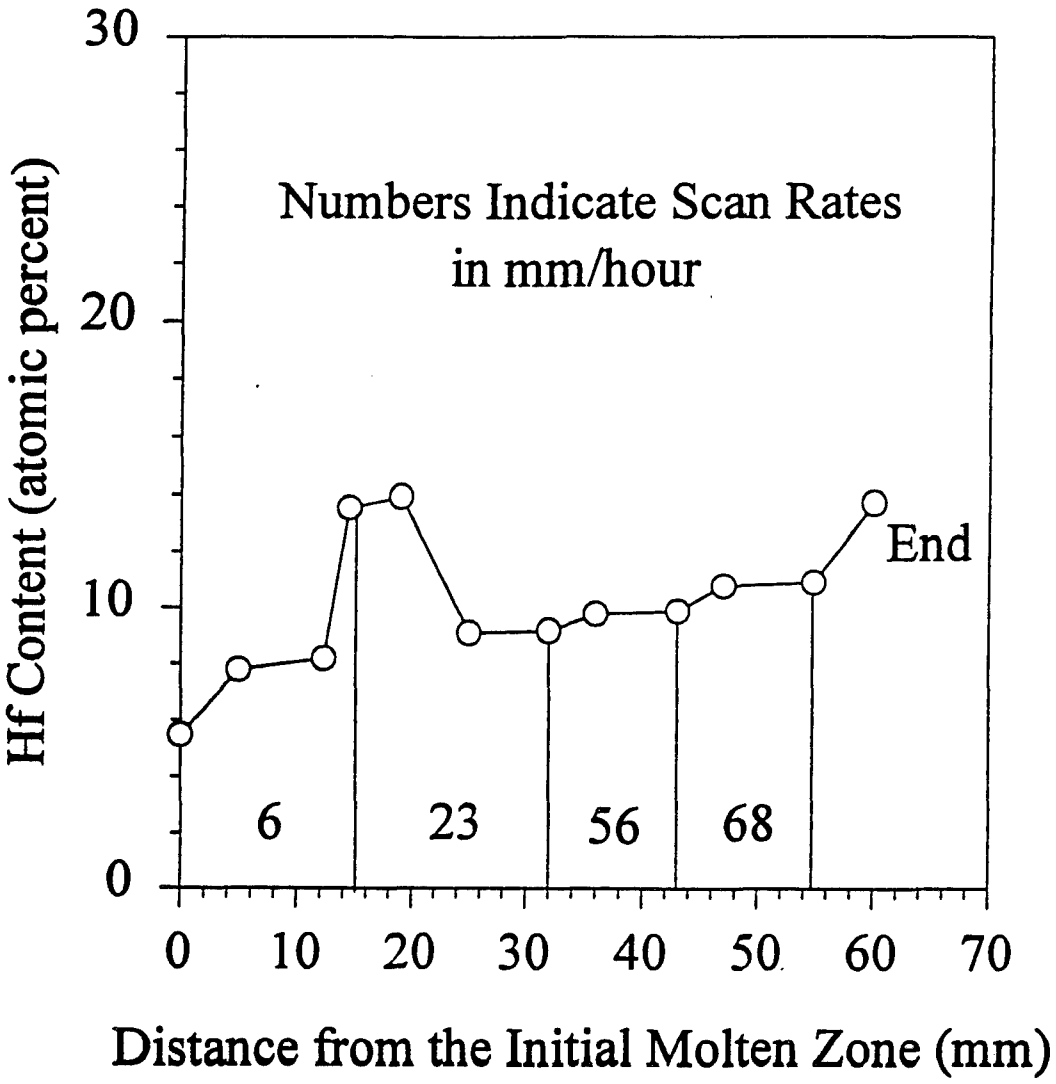

Figure 21. The composition profile in a polycrystalline Mo-10%Hf-2%C sample after first scan.

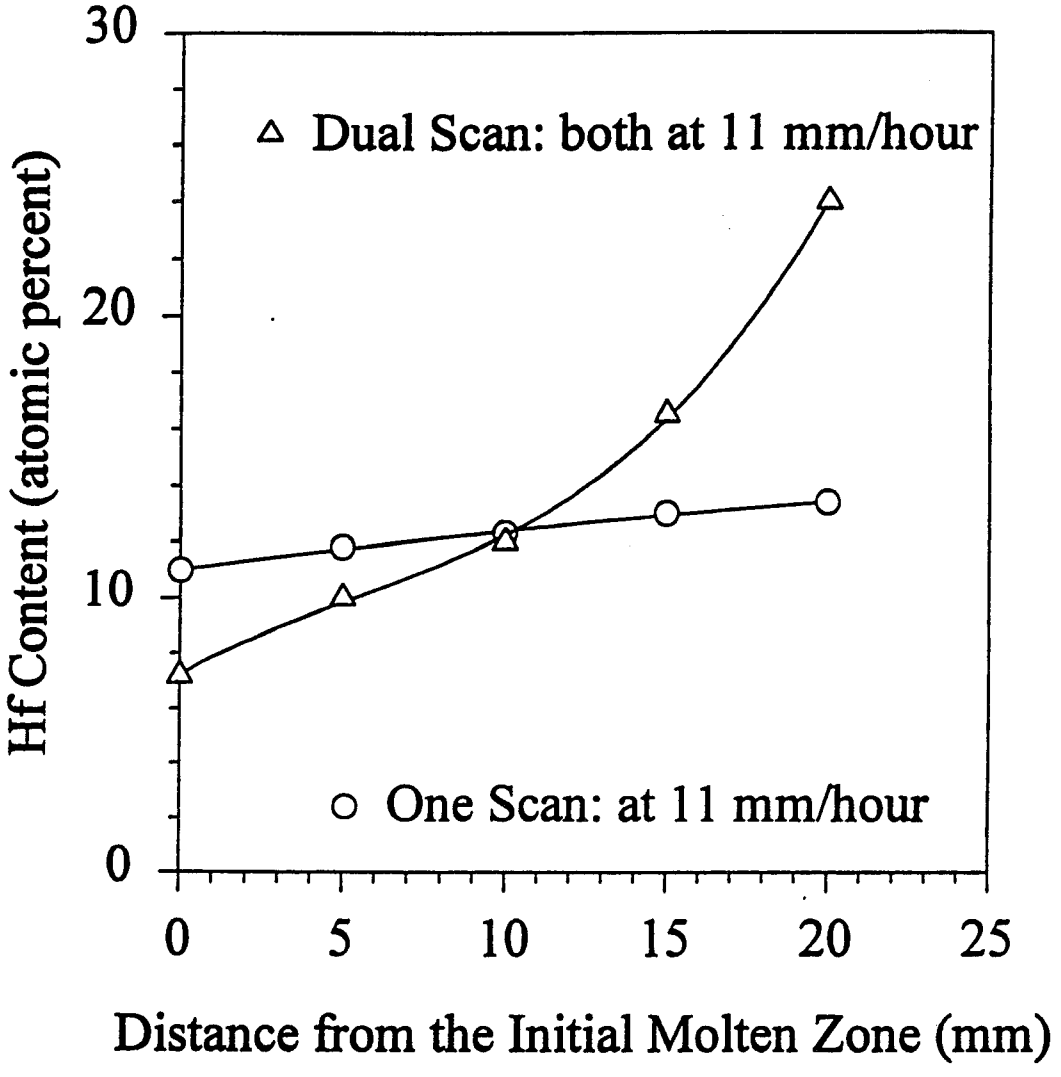

Figure 22. The composition profile in a polycrystalline Mo-15%Hf sample.

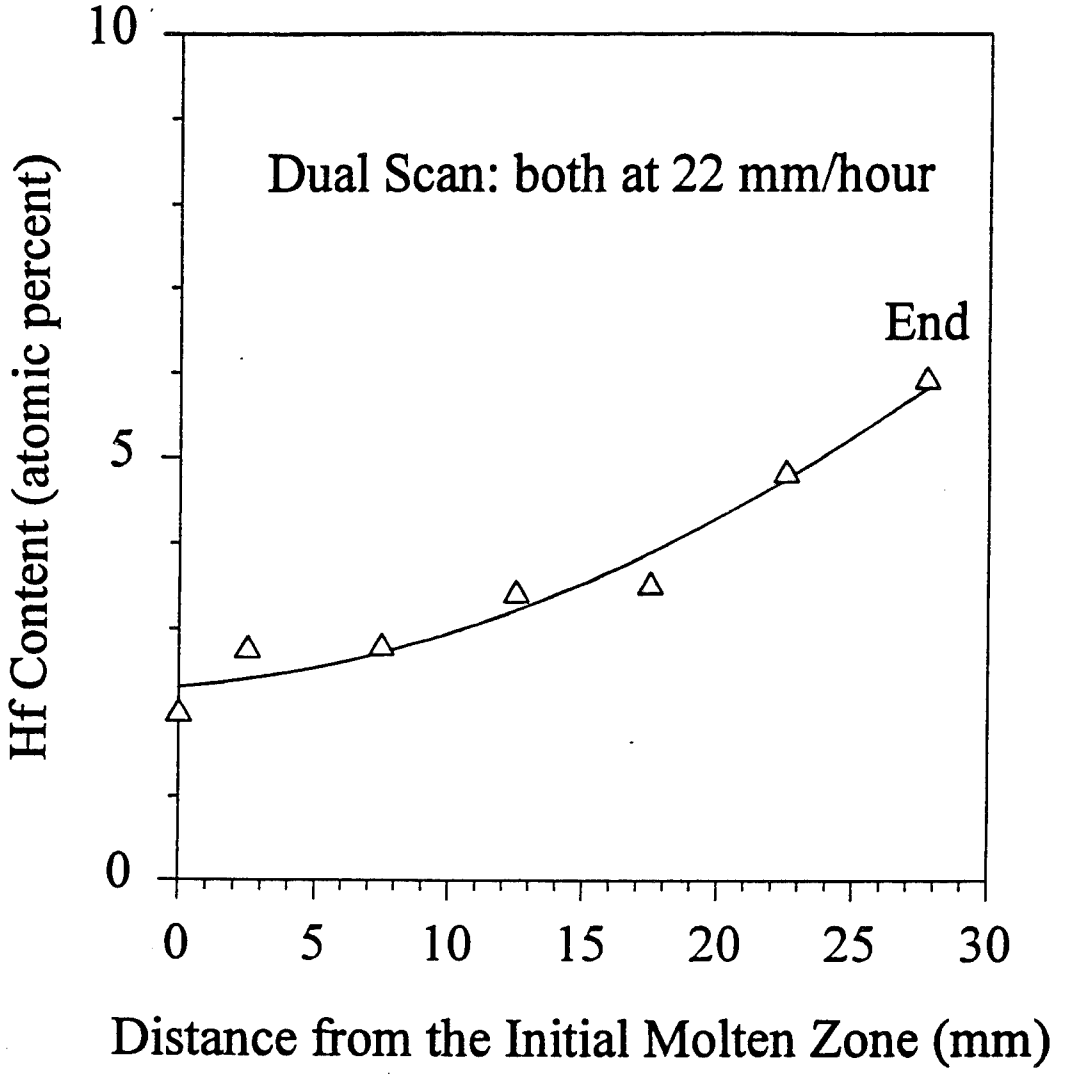

Figure 23. The composition profile in a Mo-3.71%Hf-1%C single crystal.

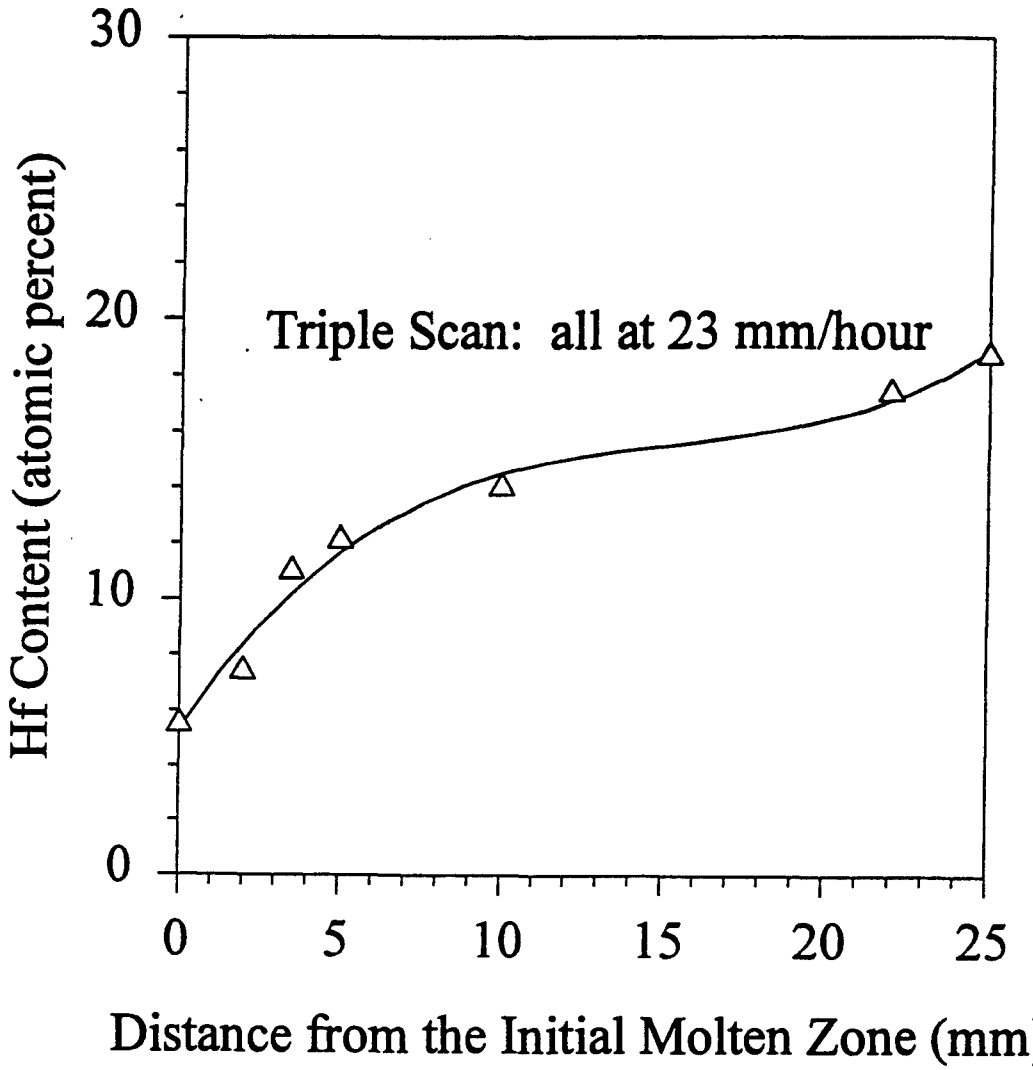

Figure 24. The composition profile in a polycrystalline Mo-10%Hf-2%C sample.

sub-boundaries was found to depend on scan rate. The sub-boundaries are thermodynamically unstable and the slower scan rates provide the time required to annihilate these boundaries. Therefore, slower scan rates result in better quality crystals with a smaller amount of boundaries.

Pre-cast rods have less gas content and higher density than the rods made by the powder metallurgical method. It is anticipated that using pre-cast rods could significantly reduce the out-gassing problem encountered using the sintered materials. As indicated above, out-gassing always disturbs the heating process and thus affects solidification and crystal quality. Numerous cavities were found on the liquid-solid interface of the raw materials made by the powder metallurgy method and the presence of these cavities was direct evidence of the problems associated with the porosity of the sintered rods. Therefore the use of pre-cast raw materials can substantially minimize the porosity problem and reduce the number of scans required. Their use should also minimize solute segregation due to the reduction in zone refining at high scan rates. A series of experiments were conducted using pre-cast rods. Figure 25 shows the microstructure of the heat affected zone of the materials processed from a pre-cast rod. The cavity problem was found to be significantly reduced. No cavities were present either in the heat affected zone or the fusion zone in most crystals formed from pre-cast rods. Only isolated cavities (very low density) were found in certain crystals.

The quality of the crystals depends on the design of electron beam gun. The electron beam gun design shown in figure 13 places the molten zone and the electron filament on different horizontal levels. But this design cannot efficiently eliminate the effects of the out-gassing of the gaseous species and the evaporation of the metal vapor that

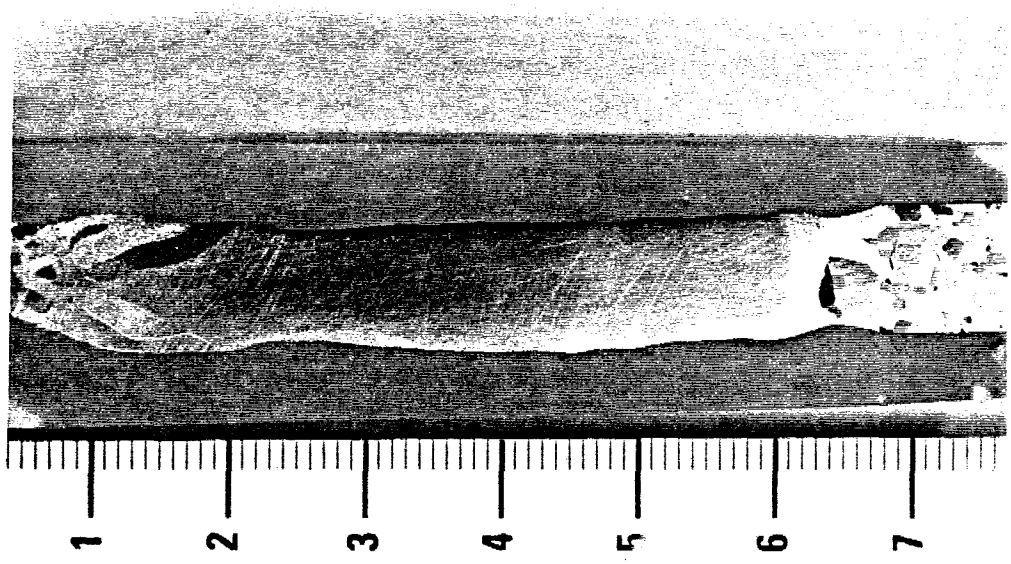

Figure 25. Microstructure of the heat affected zone of a pre-cast Mo rod (scale is centimeter).

directly affect the resistance between the anode rod and the filament. This variation in resistance causes current fluctuations and unstable heating. In the extreme case, excess current variations lead to abrupt shutdown of the power supply. Consequently, the melting ability of the system was limited to Mo rods less than 10 mm in diameter. A new electron beam gun was designed to alleviate this instability problem. A schematic drawing of the new gun is shown in figure 26 and it is similar in principle to that of Glebovsky [29]. The molten zone is 25 mm below the filament. The electron beam transverses a curved path from the filament to the specimen rod. The effects of out-gassing and metal vapor were reduced significantly. The quality and melting ability of system were improved. Figure 27 shows the surface morphology of a 12.5 mm diameter pure Mo single crystal prepared with the new electron beam gun. No power shutdown occurred during the melting process. This new gun design has a lower sensitivity to the diameter of the sample rod and out-gassing. The other advantages of this approach are its good focussing characteristics and improved lifetime of the filament due to less contamination from the molten zone.

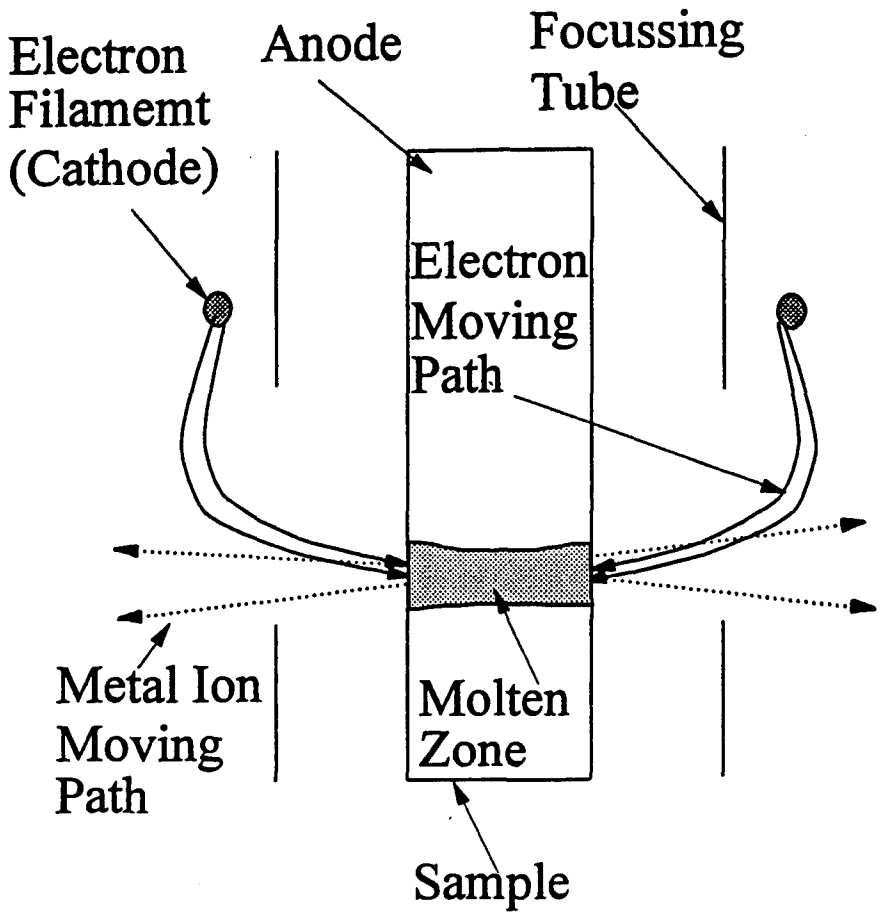

Figure 26. Schematic drawing showing the design of the improved electron beam gun.

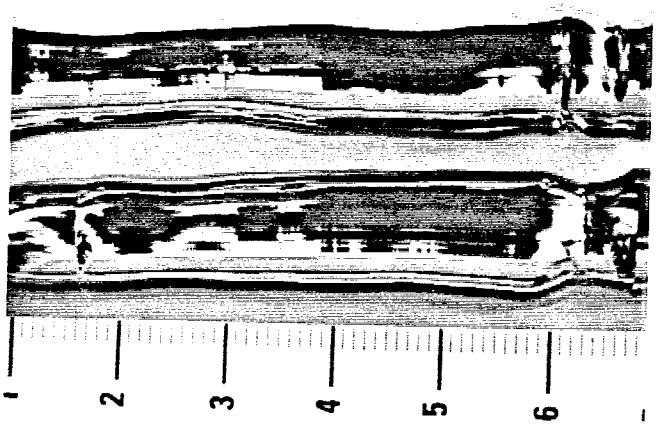

Figure 27. The surface morphology of a 12.5 mm diameter pure Mo single crystal rod prepared with the electron beam gun shown in figure 26.

4.5 CONCLUSIONS

Three types of alloys, Mo-Nb and Mo-Hf and Mo-Hf-C, were successfully grown into single crystals using an electron beam zone melting method. The growth characteristics were found to depend on the size of the two phase region of the material systems selected. Experimental results show that it is easier to grow single crystals of Mo-Nb compared to Mo-Hf and Mo-Hf-C due to the smaller temperature difference between the solidus and the liquidus lines in the former and complete solid solubility between Mo and Nb. For Mo alloys with up to 11% Nb, a high scan rate of 55 mm/hour was found to be capable of producing produce satisfactory crystals. For Mo-Hf, the optimum scan rate depends on the Hf content in an inverse manner: higher Hf contents require slower scan rates. The maximum Hf content in Mo-Hf alloys was limited to about 5% beyond which single crystals could not be formed regardless of the scan rate employed. Segregation of hafnium was observed along the growth direction and the factors controlling such an effect were examined. Experimental results indicated that the minimum scan rate for the alloys with high Hf content was about 22 mm/hour. The maximum Hf content of Mo-Hf single crystals that did not lead to significant solute segregation was 2.8%. The use of pre-cast rods was found to minimize the presence of cavities and improve the quality of the crystals produced. The use of an electron beam gun with a hidden filament could significantly improve the melting stability of the process, producing better quality crystals and enhance the lifetime of the filament.

5.0 FEASIBILITY OF PROCESSING DUCTILE BETA ALUMINA

Alumina based ceramics have attracted much attention for both electronic and structural applications; their low fracture toughness, however, is one of the obstacles to be overcome. Various toughening agents such as ZrO_2 and SiC whiskers have been tried. Results from the past studies show that zirconia can be a very good toughening agent. Na β"-alumina, which has high Na ionic conductivity, can be toughened by the addition of zirconia. This toughening is due to the transformation mechanism, namely tetragonal to monoclinic.

5.1 BACKGROUND

The zirconia addition does not significantly affect the electrical properties, as zirconia additions up to 15-20 vol% only increase the observed resistivity by about a factor of two at 300^0 C compared to commercially available pure Na β' -alumina [30-32]. Toughening is beneficial in two ways: it improves the mechanical properties of alumina, making it more robust so it does not break easily, and it increases the crack-free current carrying capacity.

Abnormal grain growth occurs during the sintering process. These large grains, which can cleave easily, serve as crack initiation sites that can limit the strength of alumina. Sintering schedules have been developed that minimize this abnormal grain growth [33]. It has been shown that adding zirconia refines the β" -alumina microstructure in the β"-alumina -zirconia composite, with additions of >7.5 vol% of zirconia preventing abnormal grain growth, leading to fine-grained, equiaxed microstructure [34]. From a practical point of view, this allows thinner composite pieces rather than pure β"-alumina ceramic to be used in electrochemical devices, which decrease the electrolyte resistance.

One failure mechanism for β"-alumina in battery applications is cracking due to pressure from the Na current that flows through the ceramic. The critical ionic current above which cracking occurs is proportional to the critical stress intensity factor(K_{Ic}) to the fourth power [35]. Thus increasing the toughness of the ceramic by a small amount can significantly increase the current carrying capacity of the ceramic. Together, the increased strength, toughness and higher critical current density of toughened β"-alumina offer promise for improving electrolyte performance in electrochemical devices, such as batteries. This very fact is the basis for the current research to improvise the fracture toughness of β"-alumina, which in turn will have wide acceptability in battery applications.

5.2 OBJECTIVES

The objectives of this work are to investigate the feasibility of fabricating more ductile beta alumina using a transformation toughening approach and subsequently examine the properties of the materials.

5.3 RESULTS FROM THE FEASIBILITY STUDY

Zirconia powder of different volume fractions was added to β"-alumina and the mixture was ball milled for 6 h to get a homogeneous mixture. This mixture was cold pressed using the CIP (Cold Isostatic Press) to obtain samples of varying diameters and lengths. The cold pressing was done at 50000psi (or 350MPa). The samples produced were further pressed at high temperatures using the Hot Isostatic Press (HIP). The HIP conditions were 1400^{0}C and 15000 psi. The samples were hipped for 1 h at the above mentioned conditions. The final sintering was done at 1450^{0}C to obtain the final samples for the subsequent mechanical and electrical testing at room temperatures and also at elevated temperatures. The final samples were found to have

densities >90% of the theoretical density. The compression and ISB (indentation strength in bending) [36] are planned to determine the fracture toughness and other mechanical properties. X-ray diffraction and SEM analysis are also planned to study the microstructure.

5.4 CONCLUSION

This is preliminary study and no concrete conclusion can be drawn at this time. However, results obtained to date indicate that the addition of ZrO_2 could enhance the fracture toughness of alumina.

6.0 SUMMARY

Efforts in this research were devoted to three aspects of materials relevant to space power systems: electrical degradation of insulators due to irradiation, processing of refractory alloy single crystals and the feasibility of fabricating ductile beta alumina. Results can be summarized as follows:

In the area of radiation indced conductivity, experimental results show that RIC in alumina consists of recoverable and permanent contributions when irradiated with charged particles. In polycrystalline alumina, a significant increase in the permanent conductivity was observed after a small incubation dose. However, only limited permanent electrical degradation was observed in single crystal samples at three times this damage level indicating the importance of grain boundaries in the radiation induced electrical degradation process. Results from Rutherford Backscattered Spectroscopy confirm that radiation enhanced diffusion of the gold contact is responsible for the degradation observed in the polycrystalline alumina specimens. In the study of single crystal, the growth characteristics in Mo-Nb, Mo-Hf and Mo-Hf-C alloys were also examined. Little difficulty was encountered when growing Mo-Nb alloys. The ease of crystal growth in Mo-Nb binary system was attributed to the small temperature difference between the solidus and the liquidus lines and the complete solid solution characteristics of the Mo-Nb system. A scan rate of 55 mm/hour was found to be suitable for producing satisfactory single crystals of Mo-11%Nb. However, for the Mo-Hf alloys, the highest scan rates for single crystal formation were found to depend on Hf content in an inverse manner. Finally, a study was conducted to determine the feasibility of fabricating more ductile beta alumina using transformation toughening of zirconia. Samples of alumina with small amounts of zirconia were fabricated based on a powder metallurgy method and preliminary results suggest that these samples possess higher fracture toughness.

REFERENCES

1. S.J. Zinkle and E.R. Hodgson, Journal of Nuclear Materials 191-194 (1992) 58.

2. G.P. Pells, Journal of Nuclear Materials 155-157 (1988) 67.

3. W.A. Ranken, T.G. Frank and G.W. Keilholtz, Thermionic Electrical Power Generation, Proceeding of the Third Conference on Thermionic Electric Power Generation (1972) 819.

4. R.W. Klaffky, B.H. Rose, A.N. Goland and G.J. Dienes, Physical Review B 21 (1980) 3610.

5. W. Keternich, F.Scheuermann and S.J. Zinkle, Journal of Nuclear Materials 206 (1993) 68.

6. P. Jung, Z. Zhu and H. Klein, Journal of Nuclear Materials 206 (1993) 72.

7. X.F. Zong, C.F. Shen, S. Liu, Z.C. Wu, Y. Chen, Y. Chen, B.D. Evans, R. Gonzalez and C.H. Sellers, Physical Review B 49 (1994) 15514.

8. E.R. Hodgson, Crystal Lattice Defects and Amorphous Materials 18 (1989) 169.

9. E.R. Hodgson, Journal of Nuclear Materials 179-181 (1991) 383.

10. E.R. Hodgson, Journal of Nuclear Materials 191-194 (1992) 552.

11. T. Shikama, M. Narni, A. Ochiai, H. Kayano and Y. Endo, Proceedings of the 15th International Symposium on Effects of Radiation on Materials. Philadelphia, PA. USA, ed. R.E. Stoller, A.S. Kumar and D.S. Gelles (ASTM STP1125) (1992) 776.

12. T. Shikama, N. Narni, Y. Endo, T. Sagawa and H. Kayano, Journal of Nuclear Materials 191-194 (1992) 575.

13. E.R. Hodgson, Journal of Nuclear Materials 179-181 (1991) 383.

14. G.P. Pells and D.C. Phillips, Journal of Nuclear Materials 80 (1979) 207.

15. G.P. Pells and D.C. Phillips, Journal of Nuclear Materials 80 (1979) 215.

16. W. K. Chu, J.W. Mayer and M.A. Nicolet, Backscattering Spectrometry (Academic Press, New York 1978).

17. E.R. Hodgson, Radiation Effects and Defects in Solids 119-121 (1991) 827.

18. E.H. Farnum, J.C. Kennedy, F.W. Clinard and H.M. Frost, Journal of Nuclear Materials 191-194 (1992) 548.

19. M.G. Houts, 27th Intersociety Energy Conversion Engineering Conference Proceedings, San Diego, CA, 2 (1992) p. 245.

20. Y.V. Nikolaev, V.S. Kolesov, P.V. Zubarev, A.G. Sintzov, N.G. Tachkova, A.A Yastrebkov, and A.S. Gontar, American Institute of Physics Conference Proceedings 271, eds., M.S. EL-Genk and M.D. Hoover, (1993) p. 267.

21. V.G. Glebovsky, V.N. Semenov and V.V. Lomeyko, J. Crystal Growth 92 (1988) 8.

22. S. Otani, J. Crystal Growth, 51 (1981) 381.

23. S. Otani, J. Crystal Growth, 51 (1981) 431.

24. S. Otani, J. Crystal Growth, 83 (1987) 481.

25. S. Otani, J. Crystal Growth, 106 (1990) 489.

26. V.G. Glebovsky, V.N. Semenov and V.V. Lomeyko, J. Crystal Growth 98 (1989) 487.

27. C.W. Lan and S. Kou, J. Crystal Growth 118 (1992) 151.

28. R. Mehrabian and A. Hellawell, Int. Met. Rev. 27 (1982) 185.

29. V.G. Glebovsky, V.V. Lomeyko and V.N. Semenov, J. of Less Common Metals, 117 (1986), 385.

30. Y.Sheng, P. Sarkar and P.S. Nicholson, Journal of Materials Science 23 (1988) 958.

31. J.G.P. Binner, R. Stevens and S.R. Tan, in "Advances in Ceramics", Vol 12, edited by N. Claussen, M. Ruhle and A.H. Heuer (American Ceramic Society, Columbus, Ohio, 1984) p.428.

32. F.F. Lange, B.I. Davis and O. Raleigh, Communication of American Ceramic Society 66 (1983) C-50.

33. G.E. Youngblood, A.V. Virkar, W.R. Cannon and R.S. Gordon, American Ceramic Society Bulletin 56 (1977) 206.

34. D.J. Green and M.G. Metcalf, *ibid.* 63 (1984) 803.

35. A.J. Virkar, Journal of Materials Science 16 (1981) 1142.

36. G.R. Anstis, P. Chantikul, B.R. Lawn and D.B. Marshall, Journal of American Ceramic Society 64 (1981) 533.

DISTRIBUTION LIST

AUL/LSE Bldg 1405 - 600 Chennault Circle Maxwell AFB, AL 36112-6424	1 cy
DTIC/OCP 8725 John J. Kingman Rd Ste 944 FT Belvoir, VA 22060-6218	2 cys
AFSAA/SAI 1580 Air Force Pentagon Washington, DC 20330-1580	1 cy
PL/SUL Kirtland AFB, NM 87117-5776	2 cys
PL/HO Kirtland AFB, NM 87117-5776	1 cy
Official Record Copy	
PL/VTP/Michael Schuller	5 cys
Dr. R. V. Wick PL/VT Kirtland, AFB, NM 87117-5776	1 cy